Numerical investigation of ice plate fractures upon rigid ball impact

Yiheng Zhang[a], Qing Wang[a *], Selda Oterkus[b], Erkan Oterkus[b], Jiabao Li[a], Duanfeng Han[a]

[a]*College of Shipbuilding Engineering, Harbin Engineering University, Harbin, 150001, China*

[b]*Department of Naval Architecture, Ocean and Marine Engineering, University of Strathclyde, Glasgow, UK*

Abstract

The fracture process and breaking capability of ice cover impacted by high-speed projectiles before underwater explosion is an urgent subject of scientific research in ice engineering applications. This paper presents the results of numerical simulations of the dynamic fracture behaviour induced by the impact of a small spherical projectile on an ice plate. The proposed 3D rate-dependent peridynamics model is validated by the dynamic ring Brazilian disc testing of ice specimens. Good agreements between the present model and the previous experiments are obtained in ice breaking processes and damage patterns of thin, medium and thick ice plates. Several cases are analysed and discussed in terms of various impact velocities, ice thicknesses, and boundary constraint conditions. The simulations identify detailed fracturing characteristics that are not observed in experiments, including the sequence and shape of crack propagation

Abbreviations: BBPD, bond-based peridynamics; In., incident bar; PD, peridynamics; SBPD, state-based peridynamics; SHPB, split Hopkinson pressure bar; Tr., transmitted bar.

* Corresponding author.
E-mail address: wangqing@hrbeu.edu.cn

in a short time interval, the crater formation and the damage evolution along the thickness direction. The proposed peridynamics computational model provides new understanding of the potential of using penetrator–ice block impact tests to observe the evolution of complex brittle damage and reveal the failure mechanism.

Keywords: Ice breaking; Peridynamics; Impact; Brittle fracture; Failure process; Penetration

1. Introduction

Ice flooding is a widespread natural disaster that has a significant effect on the safety and reliability of maritime ships, offshore platforms and cross-sea bridges near the coast. Ice breaking by underwater explosive detonation is an effective method to prevent ice jams after launching ammunition at high altitudes to penetrate the ice cover. Several studies have been published describing fragmentation of an ice cover by an underwater explosion from blast loading (Leslie and Nelson, 1961; Barash, 1966; Mellor, 1982; Wang et al., 2018c). However, the fracture process and penetration mechanism of an ice cover impacted by a high-speed projectile before the use of underwater explosives is a subject of scientific research that must be urgently progressed. Another scenario is the development of resources and exploration for life on icy planets. Icy ocean worlds on Europa are of substantial interest to the planetary community, especially because of the potential habitability of the subsurface ocean under ice sheets (Bayer et al., 2015; Marusiak et al., 2021). Many laboratory-scale

model tests have been conducted to investigate the scientific issue of penetrator–ice impact (Lange and Ahrens, 1987; Iijima et al., 1995; Kato et al., 1995; Arakawa et al., 2000; Suzuki et al., 2016). However, the above studies focused on the dynamic behaviours of thick ice blocks due to impact by a penetrator, while few studies have examined the process of crack propagation in thin or medium-thick ice plates under impact loading. Moreover, the above studies lacked effective numerical methods to accurately capture the dynamic fracture and fragmentation characteristics of ice under impact loading.

The simulation of ice material fragmentation is a challenge in computational mechanics research, and many methods have been applied to the ice numerical modelling. The most common approach, the finite element method (FEM) is widely used to evaluate the failure behaviours and load features of ice cover in ice-structure interaction (Wang and Derradji-Aouat, 2010; Millan and Wang, 2011; Kim et al., 2013; Lee et al., 2013; Kim et al., 2014), but the difference between the continuity assumption and discontinuous displacement field along the ice cracks caused the difficulty in dealing with the complicated discontinuous dynamic problems, including predicting the dynamic crack propagation and revealing the failure mechanisms. The development of meshfree methods on ice fracture mechanics and ice-structure interaction has become a newly popular research approach, such as Discrete Element Method (DEM) and Smoothed Particle Hydrodynamics (SPH). Jou et al (2019) predicted the failure modes of floe-ice and ice cakes when loaded by a moving ice-breaking ship bow based on the bonded DEM simulations, which proved that the method has potential application value

in investigating the behaviour and fracture of sea ice and the performance of icebreaker ships. Long et al (2021) exploited DEM to investigate the breaking characteristics of ice cover and ice load on upward–downward conical structure. The study found that ice cover is prone to appear local crushing failure while contacting with the junction of upward–downward cone, but it has almost no influence on the maximum ice load. DEM has advantages for modelling the discontinuous phase of the fracture process, but accuracy problems during the continuous phase make it unreliable for simulating the whole process from continuous to discontinuous. Zhang et al (2019) presented a Drucker–Prager plasticity SPH model to explore ice-ship interactions and ice failure process, and the simulation results are in good agreement with the experimental results of the Araon icebreaker model. Recently, Zhang et al (2023a) established a two-way coupling SPH model to simulate wave-induced breakup of ice floes. The results revealed that the length of broken ice piece decreases with increasing solitary wave height, and the ice floe is easier to breakage and shattered into more pieces under the action of the focused wave groups than solitary waves. However, SPH method requires external crack growth criteria to simulate damage (Madenci and Oterkus, 2013).

Over the past two decades, there have been sustained research activities on the use of a nonlocal meshless method called the peridynamics (PD) method. The bond-based peridynamics (BBPD) method was first proposed by Silling (2000) and provides an effective and viable method for modelling impact damage. Differential equations are replaced with spatial integral equations in PD, making it more suitable for solving discontinuous problems, especially the nucleation and propagation of cracks in brittle

materials. Han et al. (2019) and Javili et al. (2019) systematically reviewed the basic theory, applications and development trends in various fields, including static and dynamic failure, constitutive models of materials, fatigue problems and multi-physics coupling models. Moreover, the computational efficiency and multiphase interaction in PD are gradually being improved by coupling PD with the finite element method (Sun and Fish, 2021; Liu et al., 2022a), extended finite element method (Liu et al., 2020b), cohesive zone model (Yang et al., 2020), smoothed particle hydrodynamics (Ren et al., 2015; Fan et al., 2016) and boundary element method (Kan et al., 2020).

Dynamic fractures produced in brittle material plates upon impact by a rigid penetrator are one of the most active research topics in BBPD. Silling and Askari (2005) first predicted fragmentation with the formation of small debris when a brittle polymer-modified binder disk is impacted by a rigid ball, which proved that BBPD had the potential to address complex penetration and damage problems. Oterkus et al. (2012) demonstrated the applicability of PD simulations to assess the damage behaviour and residual strength of a concrete panel with steel reinforcements during impact loading. Hu et al. (2013) extended BBPD to a two layered glass–polycarbonate system, captured images of damage paths on the strike surface and the back surface, and found that the evolution of damage in brittle materials was sensitive to fixed boundary conditions. Bobaru et al. (2012) and Ha (2020) explored the dynamic fracture of multi-layered brittle glass plates caused by high-velocity impact and analysed the interfacial interactions between layers under stress waves. Levine et al. (2014) exploited BBPD theory for graphical modelling and realistic animation of fracture development in brittle

materials. Ren et al. (2017) reformulated the BBPD governing equation under a discontinuous Galerkin weak form and established a corresponding numerical approach for the fracture of glass layers by high-speed impact. Ma et al. (2021) focused on the variation in energy absorption characteristics with the thickness and angle of the glass plate. Recently, Anicode et al. (2020) adopted a new frictional stick-slip contact algorithm to simulate single and multiple impacts of sand particles on a zinc sulfide plate, and the final failure results were basically consistent with the available experimental studies. Chu et al. (2020) presented a rate-dependent BBPD model to investigate the fracture mechanism for ceramics during ballistic impact, and the rotation effect of bonds was further considered by Liu et al. (2022b) for simulations of fracturing when a steel column impacts a silicon carbide ceramic target. Silling and Fermen-Coker (2021) demonstrated the ability of the BBPD model to simulate the perforation of brittle elastic membranes. However, BBPD describes the interaction between material points by simply using a single elastic "spring" and thus leads to a fixed Poisson's ratio of 1/4 in 3D or 1/3 in 2D (Madenci and Oterkus, 2013).

This issue has been addressed by means of a generalized formulation referred to as state-based peridynamics (SBPD) (Silling et al., 2007; Fan et al., 2023). SBPD method is no longer regarded as a simple spring, but only the concept of pairwise force densities, which is defined as the force state. A major difference with BBPD is that the interaction between two material particles in SBPD not only depends on the deformation of the pairwise force, but also the deformation of other material particles connected to these two material particles. Thus, SBPD method can account for the

volume deformation of material and establish a closer relationship with traditional continuum mechanics theory, which can break the limitation of Poisson's ratio. However, this has led to relatively complicated implementation and expensive computational costs. The BBPD method is simpler and can be used in more stable simulations of crack propagation compared to the SBPD method, especially in cases of catastrophic fragmentation. Moreover, Poisson's ratio has notably less influence on the crack propagation speed or path when utilizing PD to simulate impact damage problems (Silling et al., 2007; Ha and Bobaru, 2010; Hu et al., 2013). Therefore, BBPD is employed in our study, and the Poisson effect is not discussed.

In the field of ice mechanics, BBPD has been widely applied to laboratory-scale S2 ice homogenization theory (Li et al., 2022; Li et al., 2023), modelling of polycrystalline ice (Lu et al., 2020), medium-scale polar ice engineering problems such as the interaction between ships (Liu et al., 2018; Wang et al., 2018b) or offshore structures (Liu et al., 2017) and ice, ice breaking by explosions (Wang et al., 2018c), thermal shocks (Song et al., 2020; 2021; 2023), propellers (Wang et al., 2018a), and bubbles (Kan et al., 2020). Few PD studies have investigated the dynamic fragmentation of ice plates under impact. In one of the earliest studies, Song et al. (2018) modified a Drucker–Prager plasticity SBPD model to provide a preliminary description of impact-induced fragmentation of thin ice plates, but the eventual failure results did not show obvious radial and circumferential cracks. Later, Song et al. (2019) extended the model with adaptive particle refinement to simulate the crater impact test of ice blocks. Recently, Liu et al. (2020a) simulated the ice–water interactions of a rigid ball

impacting a floating ice plate by coupling PD with updated Lagrangian particle hydrodynamics, and captured the dynamic ice breaking process, which produced first circumferential cracks and then radial cracks. Ren and Zhao (2022) proposed a new coupling model based on BBPD, the volume-of-fluid method, and the boundary data immersion method, which investigated crack propagation in an ice cover, the evolution of cavity shape, and the motion of spheres during ice breaking and water entry. However, none of the above studies were based on experiments, and none addressed the process of crack propagation in ice plates along the thickness direction. More recently, Zhang et al. (2023b) conducted systematic experimental studies on the effects of impact velocity and ice thickness on fracture modes and damage mechanisms. However, it was not possible to observe cracks along the thickness direction due to obstruction by the fixture, so there is a need to further explore the related damage mechanism.

The remainder of this paper is organized as follows: In Section 2, the PD methodology is briefly introduced, including BBPD theory, the failure criterion, the contact model and the validation of the proposed model. Section 3 describes the modelling and failure mode analysis for a rigid ball penetrating an ice plate, including the establishment and analysis of the penetration model, comparison of numerical and experimental results for failure processes, and discussion of the factors influencing the final damage morphology. Finally, Section 4 summarizes some concluding remarks.

2. Numerical methodology

2.1 Bond-based peridynamics theory

PD is a reformulation of elasticity theory for discontinuities and long-range forces; the discrete version of PD may be viewed as macroscale molecular dynamics in a continuum situation. For BBPD, the equation of motion of the particle marked by x in the reference configuration at time t (shown in Fig. 1) is:

$$\rho\ddot{\mathbf{u}}(\mathbf{x},t)=\int_{H_{\mathrm{x}}}\mathbf{f}(\mathbf{u}(\mathbf{x}',t)-\mathbf{u}(\mathbf{x},t),\mathbf{x}'-\mathbf{x})dV_{x'}+\mathbf{b}(\mathbf{x},\mathbf{t}) \tag{1}$$

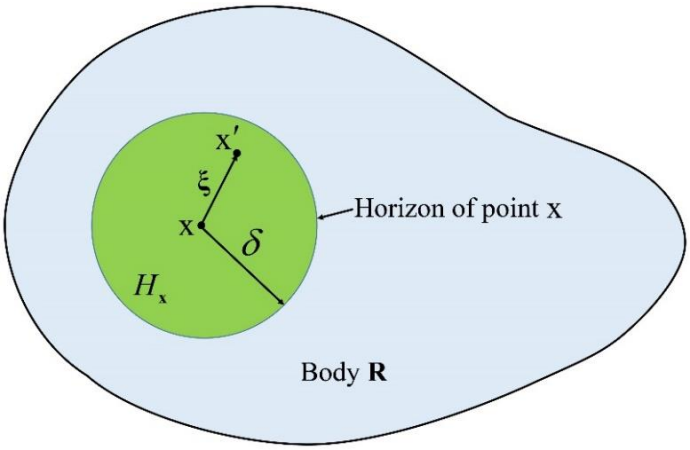

Fig. 1. Interaction between material points through bonds in the sphere H_{x}.

where ρ is the material density, $\mathbf{u}$ is the displacement vector field, $\boldsymbol{b}$ is the body force density, $V_{x'}$ is the volume of point $\mathbf{x}'$, $H_{\mathrm{x}}=\{\mathbf{x}'\in\mathbf{R}:\|\mathbf{x}'-\mathbf{x}\|\le\delta\}$ represents the collection of other material points within the horizon range, δ is the radius of the horizon, and $\boldsymbol{f}$ is the constitutive force function whose value represents the interaction force density between material points $\mathbf{x}$ and $\mathbf{x}'$ at time t. The corresponding pairwise force density is derived as:

$$\mathbf{f}(\boldsymbol{\xi},\boldsymbol{\eta})=\frac{\boldsymbol{\xi}+\boldsymbol{\eta}}{|\boldsymbol{\xi}+\boldsymbol{\eta}|}cs\mu(t,\boldsymbol{\xi},\boldsymbol{\eta}) \tag{2}$$

where $\boldsymbol{\xi}=\mathbf{x}'-\mathbf{x}$ is the relative position in the reference configuration, and $\boldsymbol{\eta}=\mathbf{u}'-\mathbf{u}$ is the relative displacement between two material points, $\mathbf{x}$ and $\mathbf{x}'$. The function c

is called the micromodulus function and represents the bond elastic stiffness, and the 3D formulation can be derived according to the literature (Rädel and Willberg, 2018):

$$c=\frac{18K}{\pi\delta^4} \tag{3}$$

where K is the bulk modulus. s is the bond relative elongation defined as:

$$s=\frac{|\boldsymbol{\xi}+\boldsymbol{\eta}|-|\boldsymbol{\xi}|}{|\boldsymbol{\xi}|} \tag{4}$$

The damage model in PD consists of breaking the PD bond connecting any two nodes when the relative change in distance between them exceeds a certain prescribed value s_0. The critical relative elongation is obtained as follows (Li et al., 2018):

$$s_0=\sqrt{\frac{5G_0}{6E\delta}} \tag{5}$$

where G_0 is the mode I critical energy release rate. E is the elastic modulus. The following bond failure criterion is introduced:

$$\mu(t,\boldsymbol{\xi},\boldsymbol{\eta})=\begin{cases}1, s<s_0\\ 0, s\geq s_0\end{cases} \tag{6}$$

The damage index D is described as:

$$D(\mathbf{x},t)=1-\frac{\int_{\mathbf{Hx}}\mu(\mathbf{x},t,\boldsymbol{\xi},\boldsymbol{\eta})dV_{x'}}{\int_{\mathbf{Hx}}dV_{x'}} \tag{7}$$

The value of $D(\mathbf{x},t)$ is between 0 and 1, and the closer it is to 1, the greater the degree of ice damage.

2.2 A rate-dependent failure model of ice

In the present study, a new failure model is implemented to simulate the dynamic

fracture of ice in response to an impact. The model considers the rate effect on the fracture toughness of ice. The crack growth occurs when the stress intensity factor at the crack tip is larger than the fracture toughness of the ice material. This is expressed by:

$$K_I > K_{Ic} \tag{8}$$

Zhang et al. (2021) explored the dynamic fracture toughness K_{Id} of freshwater ice using a modified split Hopkinson pressure bar (SHPB) devices at temperatures ranging from –5°C to –45°C. The results revealed a linear relationship between the normalised dynamic loading rate $\dot{K}_{Id} / K_{Ic0}$ and normalised dynamic fracture toughness K_{Id} / K_{Ic0}. Here, the dynamic loading rate ($\dot{K}_{Id}$) is determined by fitting the slope of the rising part of the stress intensity factor history curve. For the normalised loading rate below a critical value, the toughness fracture K_{Ic} is represented by a constant quasi-static toughness fracture K_{Ic0}; for the normalised loading rate above the critical value, the normalised dynamic toughness fracture increases approximately linearly with increasing the normalised dynamic loading rate (Zhang et al., 2021). Fig. 2 shows the fitting results at –15°C.

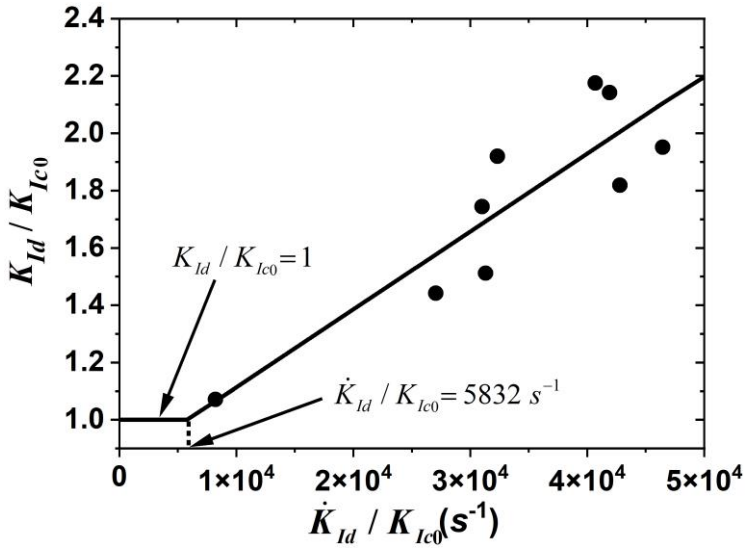

Fig. 2. Normalised dynamic fracture toughness as a function of the normalised dynamic loading rate of freshwater ice at −15°C (data from Zhang et al. (2021)).

The normalised dynamic fracture toughness, K_{Id} / K_{Ic0}, is described by:

$$K_{Id} / K_{Ic0} = \begin{cases} 1 & (\dot{K}_{Id} / K_{Ic0} < 5832\ s^{-1}) \\ 0.84141 + 2.7193 * 10^{-5} \dot{K}_{Id} / K_{Ic0} & otherwise \end{cases} \tag{9}$$

The relative stretch rate of the bond $\dot{s}$ according to the literature (Liu et al., 2022b) is:

$$\dot{s} = \frac{\dot{\boldsymbol{\eta}} \cdot (\boldsymbol{\xi} + \boldsymbol{\eta})}{|\boldsymbol{\xi}| \cdot |\boldsymbol{\xi} + \boldsymbol{\eta}|} \tag{10}$$

Notably, some researchers assumed $\dot{s}$ as the strain rate of material points to establish failure models while considering tensile strength (Zhu and Zhao, 2021) and compression strength (Liu et al., 2022b) rate effects in PD. In this study, $\dot{s}$ is considered approximately equal to the normalised dynamic loading rate. The numerical results of the two rate-dependent models of ice are initially compared in Section 3.1.3. G_0 in Eq. (5) can be expressed by fracture toughness under plane strain condition, that is, $G_0 = (1-\nu^2) K_{Ic}^2 / E$ (Toussaint and Polyzois, 2019). The derivative of Eq. (5) can be

expressed as:

$$s_0 = \frac{K_{Ic}}{E}\sqrt{\frac{5(1-\nu^2)}{6\delta}} \tag{11}$$

2.3 Contact model

An algorithm for contact-impact between a rigid body and a deformable body was described in Madenci et al. (2014); it is suitable for the contact interaction between a rigid projectile and a target structure. At a particular time step t, the rigid impactor moves with an initial velocity v, as shown in Fig. 3a. After contact occurs between the impactor and target material at time $t+\Delta t$, there is initial interpenetration of material points, as illustrated in Fig. 3b. To reflect this physical reality, the material points inside the impactor are relocated to their new positions outside the impactor (see Fig. 3c). For a rigid sphere, the particles in the region where contact occurs are pushed to the closest surface along the radius of the sphere. The velocity of such a material point, $\mathbf{x}_{(k)}$, in its new location at the next time step, $t+\Delta t$, can be computed as

$$\overline{\mathbf{v}}_{(k)}^{t+\Delta t} = \frac{\mathbf{u}_{(k)}^{t+\Delta t} - \mathbf{u}_{(k)}^{t}}{\Delta t} \tag{12}$$

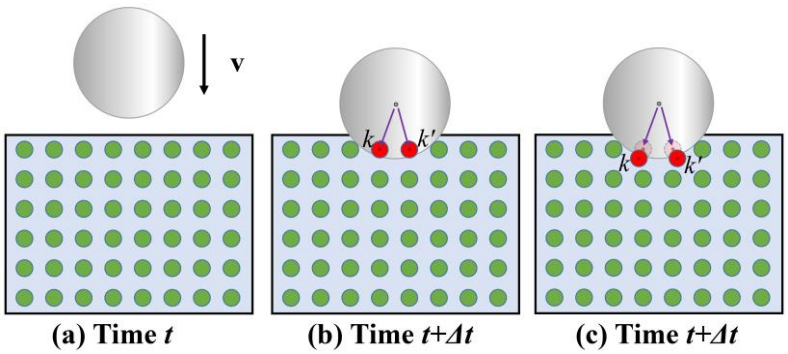

Fig. 3. Relocation of material points inside a deformable target to represent contact with

a rigid impactor.

Thus, at time step $t+\Delta t$, the force exerted on the impactor by point $\mathbf{x}_{(k)}$ is:

$$\mathbf{F}_{(k)}^{t+\Delta t} = -\rho_k \frac{\overline{\mathbf{v}}_{(k)}^{t+\Delta t} - \overline{\mathbf{v}}_{(k)}^{t}}{\Delta t} V_{(k)} \tag{13}$$

At time step $t+\Delta t$, the total force of the impactor can be computed from:

$$\mathbf{F}^{t+\Delta t} = \sum_{k=1} \mathbf{F}_{(k)}^{t+\Delta t} \lambda_{(k)}^{t+\Delta t} \tag{14}$$

where:

$$\lambda_{(k)}^{t+\Delta t} = \begin{cases} 1 & \text{inside impactor} \\ 0 & \text{outside impactor} \end{cases} \tag{15}$$

2.4 Validation of numerical simulation

To verify the effectiveness of the numerical model, the ring Brazilian disc ice test is performed using an improved SHPB (as shown in Fig. 4a).

Similar to previous studies (Zhang et al., 2021; Zhang et al., 2023c), ring Brazilian disk granular ice specimens with an outer diameter of 70 mm, an inner diameter of 20 mm, and a thickness of 15 mm are specially prepared in cylindrical silica gel moulds and processed at –15°C in cold storage. The material parameters of the ice adopted in this case are as follows: Young's modulus E = 10 GPa, Poisson's ratio v = 0.25, density 897 kg/m^3, and quasi-static fracture toughness 184.9 $kPa \cdot m^{1/2}$ (Zhang et al., 2021).

The basic assumption of the SHPB device is to satisfy one-dimensional stress wave theory. Therefore, we adopted the modelling method for the SHPB test proposed by Gu et al. (2016). Fig. 4b shows the model for the calculation of ice in the SHPB after PD dispersion. The striker bar, incident bar and transmitter bar are made of aluminium

alloy, with a Young's modulus of 68.9 GPa and a density of 2,750 kg/m^3. The lengths of the striker bar and incident bar with a diameter of 60 mm are 0.45 m and 3.3 m, respectively. To increase the magnitude of weakly transmitted signals, a hollow transmitted bar is adopted with an outer diameter ϕ of 60 mm, an inner diameter ψ of 40 mm, and a length of 2.42 m.

The PD simulation measures the strain–time relationship at the position of the two strain gauges. The striker bar moves with an initial velocity v of 3.61 m/s, and the incident bar is initially static. A rigid contact model is applied between the incident bar and specimen and between the transmitter bar and specimen. A flexible contact model is adopted between the striker bar and the incident bar. A detailed description of the contact model is available in Madenci et al. (2014) and Gu et al. (2016). The PD simulation is conducted with a material point size of dx=0.00048 m for the specimen and dx'=0.0005 m for the bars, a horizon size δ that is three times the particle point size. In BBPD, the explicit method requires a critical time step for numerical stability (Silling and Askari, 2005). Here, a time step of dt= 5.0×10^{-8} s, which is less than the critical time step for the explicit time integration.

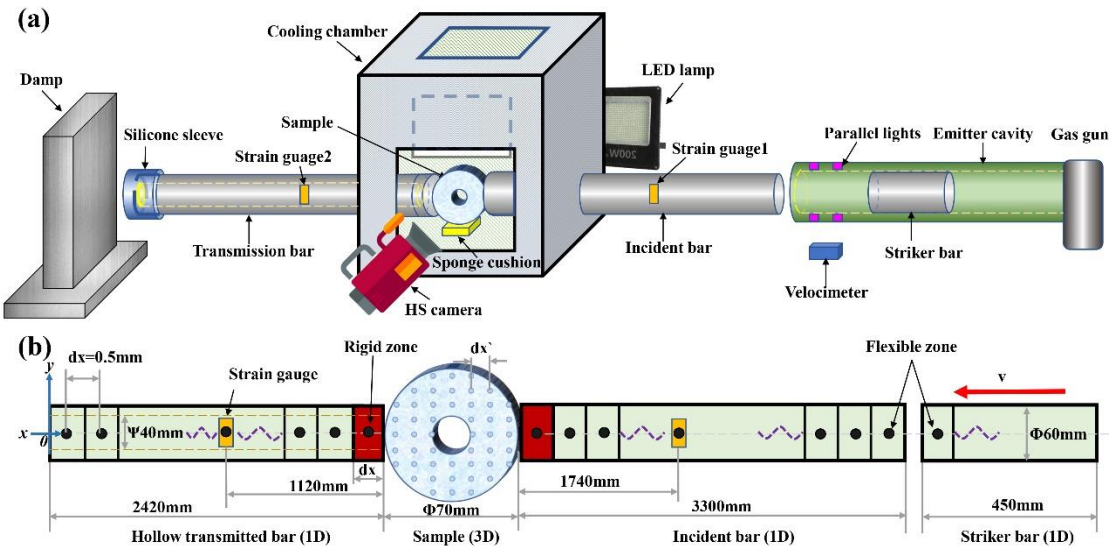

Fig. 4. Modified SHPB apparatus for the dynamic ice impact tests: (a) schematic of the SHPB device; (b) calculation model of the PD simulation.

Fig. 5 shows a comparison between the experimental and simulated results for the strain–time curves measured in the incident (In.) bar and transmitted (Tr.) bar with an impact velocity of 3.61 m/s. The incident strain and reflected strain are sine waves in the experiment but rectangular waves in the simulation. This is related to the waveform shaper technology (Zhang et al., 2020; Zhang et al., 2021) adopted in the test to make the rising edge of the incident wave smoother, which is conducive to stress balance. The error of peak transmitted strain obtained by simulation is less than 17% of the experimental value. Fig. 6 shows the progressive failure process in the experiment and numerical results for the SHPB. The PD simulation results are in good agreement with the experimental observations, which proves that the numerical simulation is reasonable and applicable.

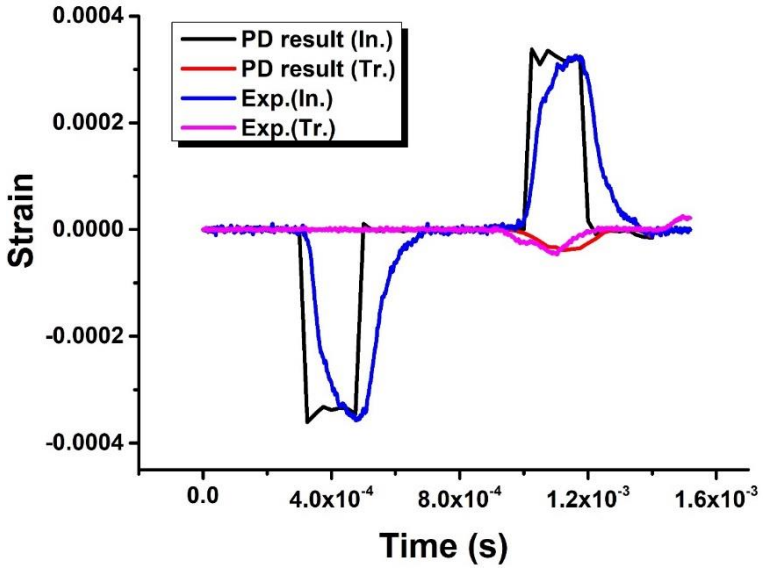

Fig. 5. Strain–time curve in the dynamic ring Brazilian disc ice test.

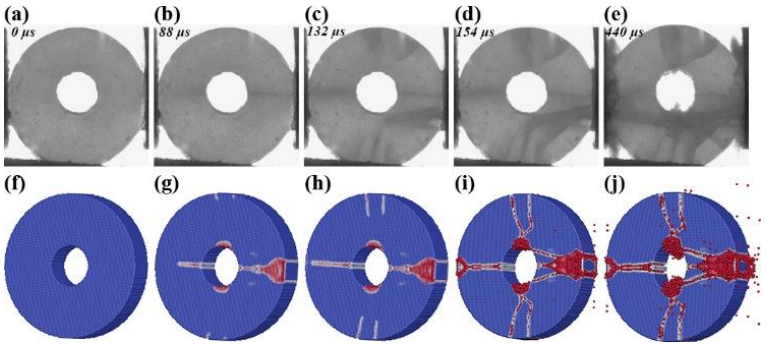

Fig. 6. The dynamic crack propagation process of a ring Brazilian disc ice specimen: (a)–(e) experimental results; (f)–(j) PD simulation results.

3. Results and discussion

3.1 Establishment and analysis of a numerical model of a rigid ball penetrating an ice plate

To enable a better comparison with the experimental results (Zhang et al., 2023b), we choose the dimensions of the ice plate and rigid ball to match those from the experiments in the literature. The diameter of the steel sphere is 15 mm, and it has a

mass of 13.99 g. The length, width and thickness of the rectangular ice plate are 0.22 m, 0.22 m and 0.01 m, respectively. The impact velocity of the rigid ball is 71.7 m/s, and the residual velocity is 60.8 m/s in the experiment (Zhang et al., 2023b). The material parameters of ice in this case are as follows: Young's modulus $E = 3.8\,GPa$, Poisson's ratio $\upsilon = 0.25$, density $\rho = 907\,kg/m^3$, and quasi-static fracture toughness 220 $kPa \cdot m^{1/2}$. We select the particle spacing of dx=1 mm and a horizon size $\delta = 4dx$ used for the discretization of the domain integral in the numerical model. The calculation time step (dt) is set to 5.0×10^{-7} s, which is approximately one order smaller than the critical time step estimated using the approach proposed by Silling and Askari (2005).

3.1.1 Applied boundary condition

In the experiment, two transparent acrylic frames with 150 mm diameter circular openings are utilised to fix the ice sample. Thus, complete boundary modelling including two acrylic plates, four screw clamps and an ABS positioning plate leads to complex calculation costs. In addition, the pressure exerted on the fixture is uncertain. Eventually, we choose two simplified fixed boundary conditions, as shown in Fig. 7. The first condition is to manually add 4-layer boundary particles at the boundary and then set its displacement and velocity in the z-direction to 0 (Fig. 7a). The other method is to treat the acrylic frames as two fixed rigid bodies, that is, set the boundary conditions through a rigid contact model (Fig. 7b).

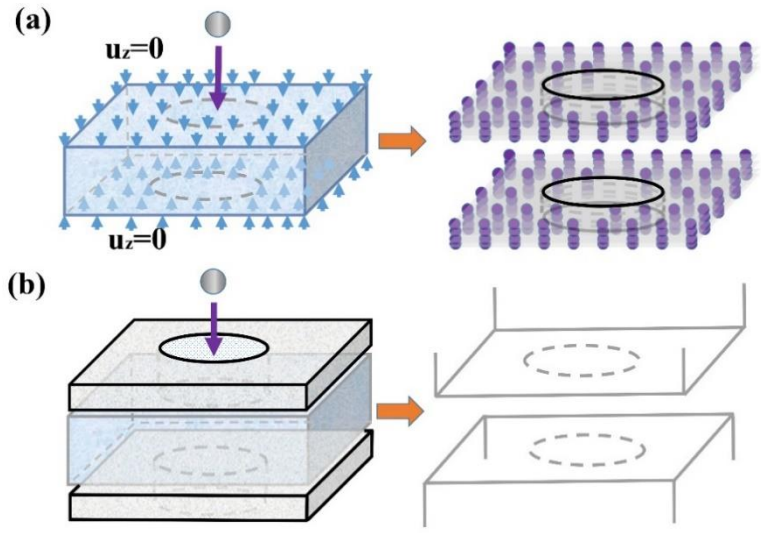

Fig. 7. Two approaches of imposing fixed boundary conditions: (a) virtual boundary layer method; (b) fixed rigid contact model.

The residual velocities obtained by the two approaches are 59.0 m/s and 60.5 m/s, with deviations of 2.96% and 0.49%, respectively, from the experiment. The results for the damage in the two approaches are shown in Fig. 8. The virtual boundary layer method leads to an obvious local damage effect at the opening of the acrylic frames, and the central main crack is severely constrained to extend to the edge of the ice plate. This issue was described and discussed by Hu et al. (2013). In the actual test, the response between the acrylic fixtures on both sides and the ice plate is more flexible, resulting in no obvious circular cracks at the opening. In contrast, the fixed rigid contact model still produces circumferential cracks near the opening, which is more consistent with the experimental results. Moreover, by using the rigid contact model instead of modeling multiple layers of virtual boundary particles, computational efficiency is further improved.

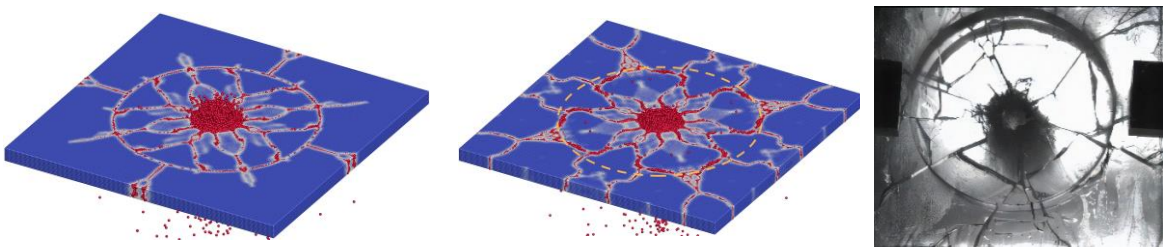

(a)virtual boundary layer method (b) fixed rigid contact model (c) experimental result

Fig. 8. Comparison of damage in PD simulations: (a) and (b) are for various applied boundary conditions; (c) experimental observations (Zhang et al., 2023b).

3.1.2 Horizon size

The dependence of crack propagation on horizon size is discussed in this section. The ratio of the neighbourhood horizon size to particle spacing is recorded as $m = \delta / \Delta x$. Six different neighbourhood horizon sizes (m =1, 2, 3, $2\sqrt{3}$, 4 and $3\sqrt{2}$) are selected for analysis and comparison. The residual velocities obtained by simulation are 68.9 m/s, 68.2 m/s, 65.6 m/s, 63.8 m/s, 60.5 m/s and 63.5 m/s, with deviations of 13.32%, 12.17%, 7.89%, 4.93%, 0.49% and 4.44%, respectively, from the test. Fig. 9 shows the numerical failure effects for different neighbourhood sizes. By comparison, four non-through-thickness radial cracks form at m =1. When m =2, multiple microcracks are generated near the centre of the ice plate. At m =3, radial cracks extend to the boundary of the ice plate, and circumferential cracks appear. However, when $3 \leq m \leq 3\sqrt{2}$, the crack propagation path is more consistent with the experimental results at m=4. Therefore, m =4 is adopted for the further study here.

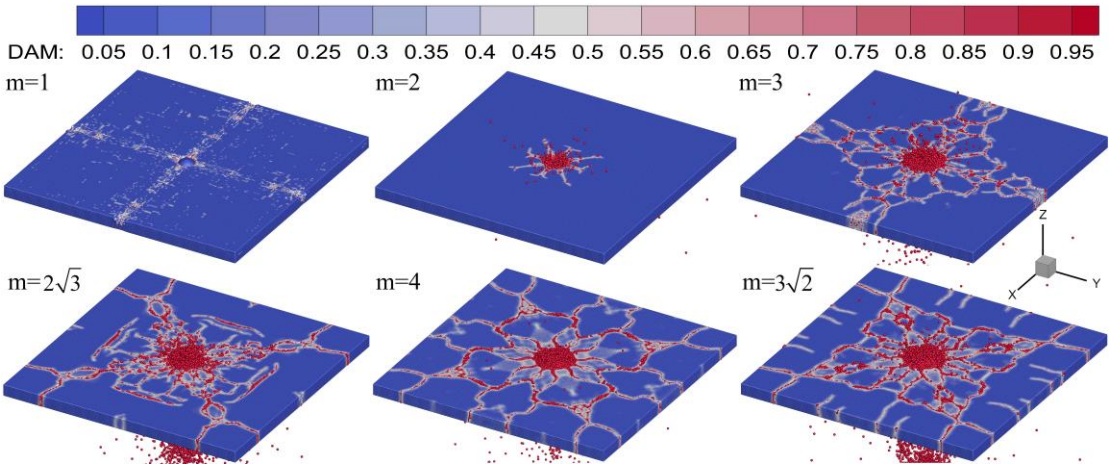

Fig. 9. The damage results of ice plates for different neighbourhood sizes ($\mathrm{m} = \delta / \Delta x$).

3.1.3 Comparison of two rate-dependent BBPD models

Compared with Eq. (5), several scholars have adopted tensile strength to describe the critical stretch (Wu et al., 2020):

$$s_0 = \sigma_{dt} / E \tag{16}$$

where σ_{dt} is the tensile strength of the material.

Experimental tests demonstrated that ice is sensitive to the strain rate (Zhang et al., 2020). Thus, it is extremely significant to consider the effect of rate for dynamic loading. The rate effect under tensile conditions was described by (Zhu and Zhao, 2021):

$$\sigma_{dt} = \begin{cases} \sigma_{st}, & (\dot{\varepsilon} \le \dot{\varepsilon}_0) \\ \exp\left[C_1 In\left(\dfrac{\dot{\varepsilon}}{\dot{\varepsilon}_0} \right) \right] \sigma_{st}, & (\dot{\varepsilon} > \dot{\varepsilon}_0) \end{cases} \tag{17}$$

where $\dot{\varepsilon}$ refers to the equivalent strain rate at a specific point as calculated in Eq. (10), and $\dot{\varepsilon}_0$ is a critical strain rate when the dynamic effect is considered. Eq. (17) essentially describes a relationship between the strain rate and tensile strength, as illustrated in Fig. 10. That is, for strain rates below $\dot{\varepsilon}_0$, the tensile strength is

represented by a constant static tensile strength σ_{st}; for strain rates above $\dot{\varepsilon}_0$, the tensile strength increases exponentially with increasing strain rate. The static tensile strength of the ice is selected to be 1.43 MPa (Petrovic, 2003). The critical strain rate $\dot{\varepsilon}_0$ is determined to be 1.04 s^{-1} in this study. Based on available experimental data for freshwater ice (Zhang et al., 2020), the constant C_1 is determined to be 0.21.

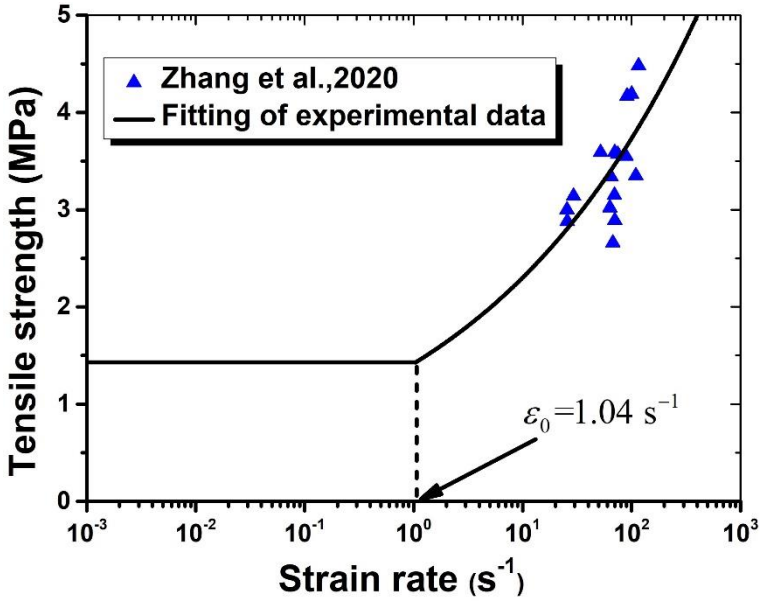

Fig. 10. The relationship between the strain rate and dynamic tensile strength of ice. Experimental data are extracted from Zhang et al. (2020).

Assuming that $\dot{s}$ is the tensile strain rate (Wu et al., 2020), the critical relative elongation can be written as:

$$s_0 = \begin{cases} scr0, & (\dot{s} \le \dot{\varepsilon}_0) \\ \exp\left[C_1 In\left(\dfrac{\dot{s}}{\dot{\varepsilon}_0}\right)\right] * scr0, & (\dot{s} > \dot{\varepsilon}_0) \end{cases} \tag{18}$$

The residual velocity obtained by the model is 62.90 m/s, with a deviation from the test of 3.45%. Fig. 11 shows the damage based on the tensile strength rate effect model. Catastrophic damage occurs in the central area and near the four boundaries of the ice plate, which is a significant discrepancy from the experimental observations (Fig.

8c). In contrast, the proposed model in this paper has better consistency.

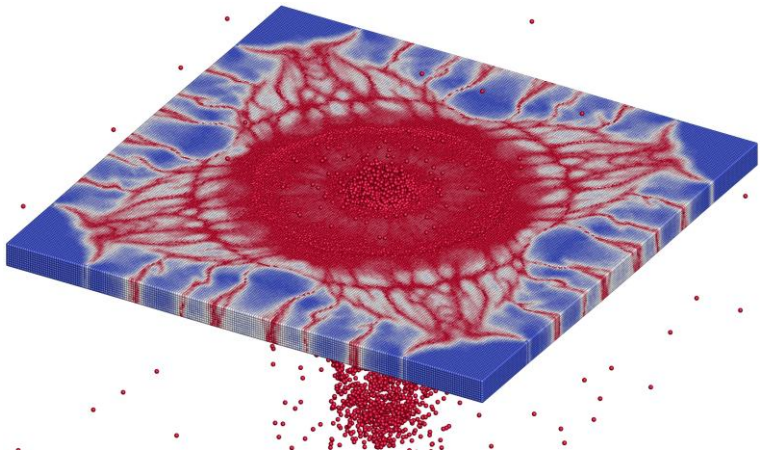

Fig. 11. The damage results of the ice plate using the tensile strength rate effect for the BBPD model.

3.2 Comparison of the numerical simulation and experimental results for the ice breaking processes

Based on the ice breaking process observed in the experiment, Zhang et al. (2023b) classified ice plates into three types according to thickness: thin (6 mm), medium (10 mm) and thick (26 mm, 36 mm and 50 mm). In this study, we simulate typical cases and compare the ice breaking process with experimental results. The moment when the projectile contacts the ice sample in the PD is selected as the initial time (0 μs).

3.2.1 Ice breaking of thin ice plates

Fig. 12 shows the failure process of a 6-mm-thick ice plate at an impact velocity of 28.8 m/s. The residual velocity obtained by simulation is 24.8 m/s, which is almost equal to the experimental measurement value of 24.6 m/s. At 50 μs, the crack formation of the ice plate on the impact surface (Fig. 12a) and back surface (Fig. 12c) is not completely consistent; only four radial cracks develop from the centre of the strike

surface, while several circumferential cracks appear on the back surface. After 50 μs, circumferential cracks initiate and converge simultaneously from two adjacent radial cracks (green arrow in Fig. 12), while radial cracks continue to extend to the edge. The model exhibits a generally consistent result on the strike surface compared to the experimental study (Fig. 12b). At 450 μs, the back view (Fig. 12c) shows that the debris in front of the rigid ball has a cylindrical shape with a hemispherical head, which demonstrates good agreement with the experimental observations (Fig. 12d).

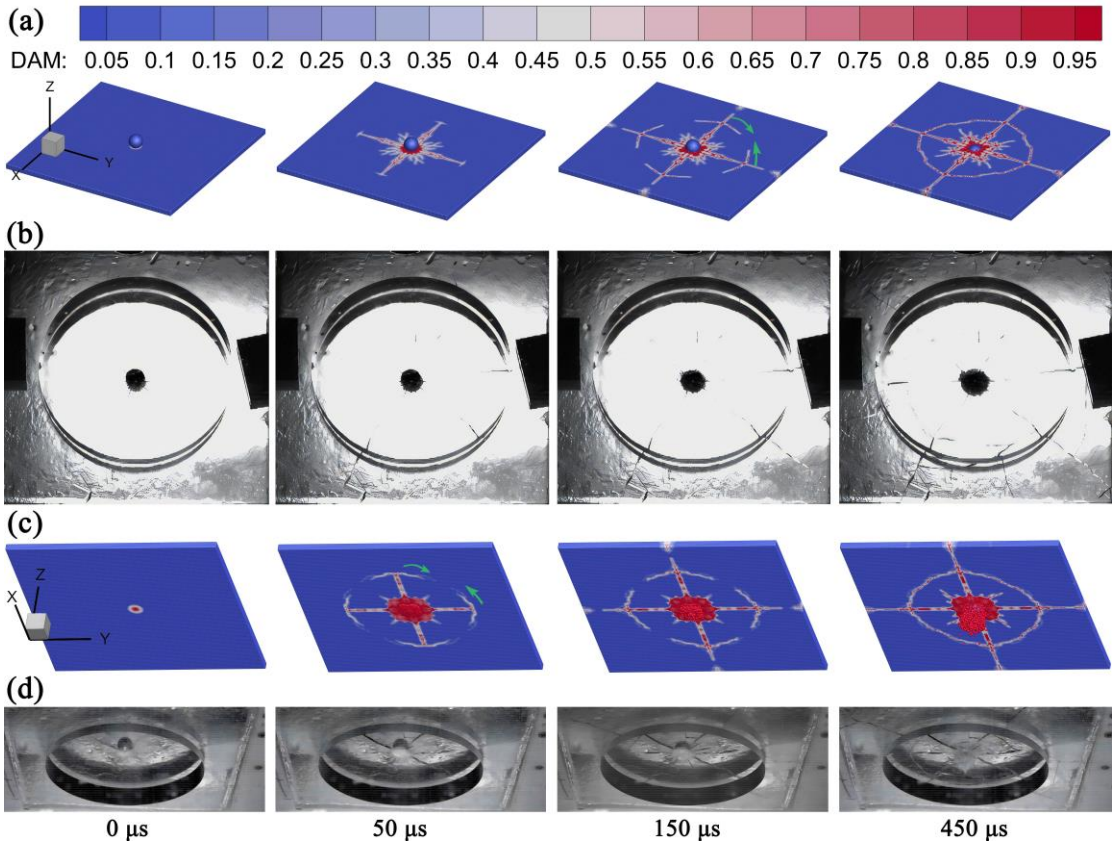

Fig. 12. Comparison of the failure processes of the 6-mm-thick ice plate at an impact velocity of 28.8 m/s: (a) and (c) PD models, and (b) and (d) experimental observations (Zhang et al., 2023b); (a)–(b) strike surfaces, and (c)–(d) back surfaces. Green arrows indicate the propagation direction of circumferential cracks.

Due to the limitations of the high-speed camera, the shortest observed time interval

is 50 μs in the experiment. The numerical method has the ability to display more detailed crack evolution in a shorter time interval. In the PD model, when the damage index D of a particle is greater than 0.5, the particle is completely disconnected from more than half of the bonds within the horizon and therefore has the potential to transform into part of the fracture surface. In this study, we define the failure process under this condition as an individual fracture surface, as shown in Fig. 13a. At contact (0 μs), damage forms in a small cylinder. Subsequently, a lower conical crater is rapidly generated at 12 μs, and four radial cracks and many microcracks appear in the centre. After 24 μs, the central high-pressure zone stops expanding, while radial cracks continue to propagate. From the cross-sectional view (Fig. 13b), we can identify that once a lower conical crater is formed, there is no significant variation in the cone angle.

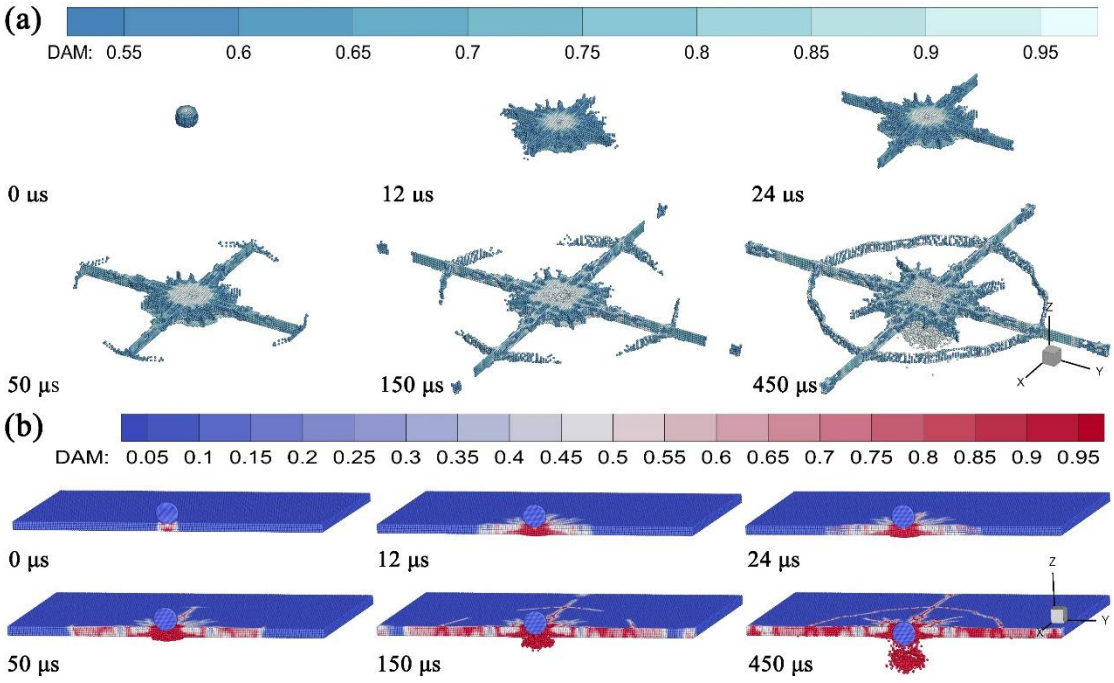

Fig. 13. Damage processes in the thickness direction of the 6-mm-thick ice plate at an impact velocity of 28.8 m/s: (a) the individual fracture surface, and (b) the cross section.

Fig. 14 shows the failure process of the 6-mm-thick ice plate at an impact velocity of 70.8 m/s. The predicted residual velocity is 65.2 m/s, which is close to the experimental measurement value of 67.1 m/s. In the experiment, the cracks on the strike surface (Fig. 14b) and back surface (Fig. 14d) exhibit apparent asymmetry, mainly due to the sophisticated interaction between the fragile thin ice plate and the frames under impact loading (Zhang et al., 2023b). In contrast, the fracture results of the PD simulation under more ideal boundary conditions show symmetry on the impact surface (Fig. 14a) and back surface (Fig. 14c). At 50 μs, petal-shaped cracks appear near the centre of the ice plate, and they are generally concentrated inside the circular opening diameter (15 mm) of the acrylic fixture. At 150 μs, the radial cracks are fully extended, and two circumferential cracks (green oval symbol) occur at some positions in Fig. 14c. In the simulations, the cracks no longer evolve at 450 μs, and the debris cloud in front of the rigid ball has a cylindrical shape with a semi-ellipsoidal head (as shown in Fig. 14c), which is very consistent with the experimental observations (Fig. 14d).

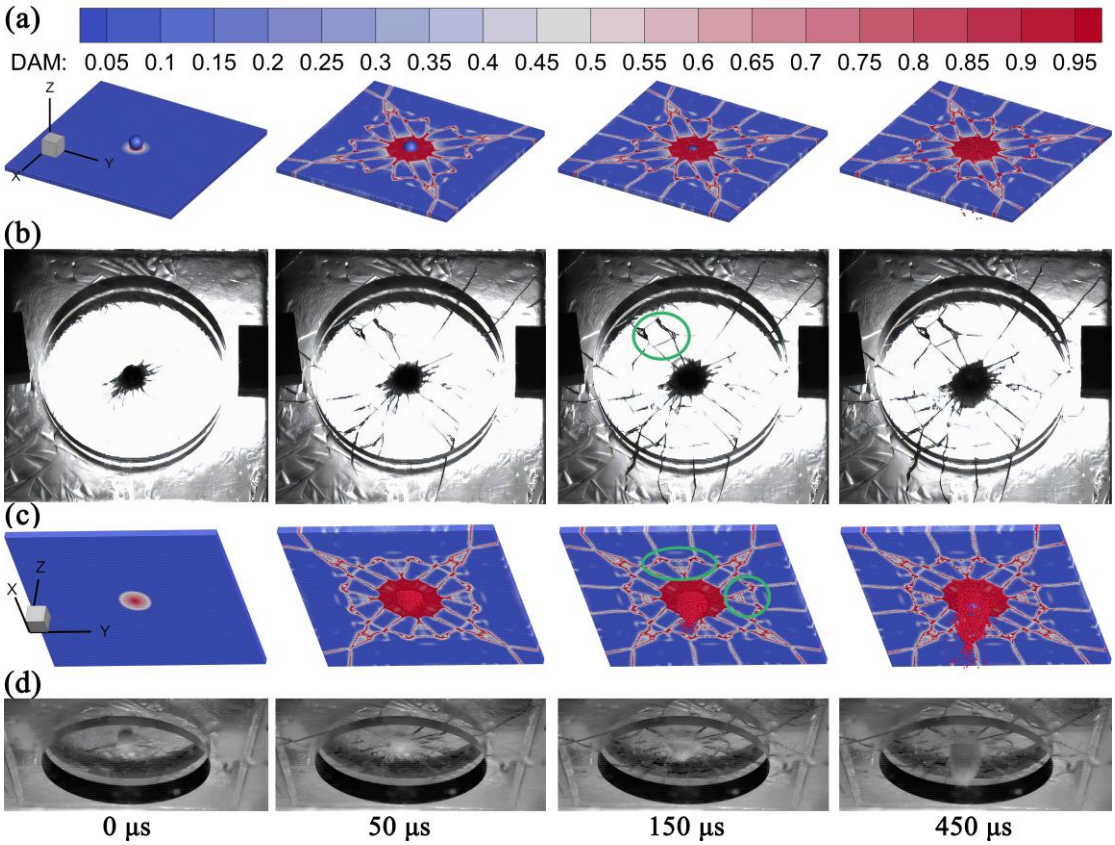

Fig. 14. Comparison of the failure processes of the 6-mm-thick ice plate at an impact velocity of 70.8 m/s: (a) and (c) PD models, and (b) and (d) experimental observations (Zhang et al., 2023b); (a)–(b) strike surfaces, and (c)–(d) back surfaces. Green oval symbols indicate the two circumferential cracks.

Fig. 15a presents individual images of the progression of damage of a 6-mm-thick ice plate at an impact velocity of 70.8 m/s. At contact, a small conical damage area forms directly, and then it instantly evolves into a zone shaped like a flat cake at 8 μs. Central radial cracks appear at 24 μs, while a small number of corner cracks form due to the reflection of the tensile wave at the corners. At 50 μs, radial cracks converge with some corner cracks, and the shape of the central crack resembles a wagon wheel with 16 spokes. As the impact velocity increases from 28.8 m/s (Fig.13b) to 70.8 m/s (Fig. 15b), the area of the high-pressure zone is significantly larger along the thickness

direction. Notably, the shape of the damage may differ at the selected cross-sectional positions. At 450 μs, the green rectangular symbol (shown in Fig. 15b) is not the crater boundary but the radial crack initiation zone outside the crater. Therefore, the top and bottom views are more conducive than the cross-sectional damage map for accurately evaluating the value of the crater diameter.

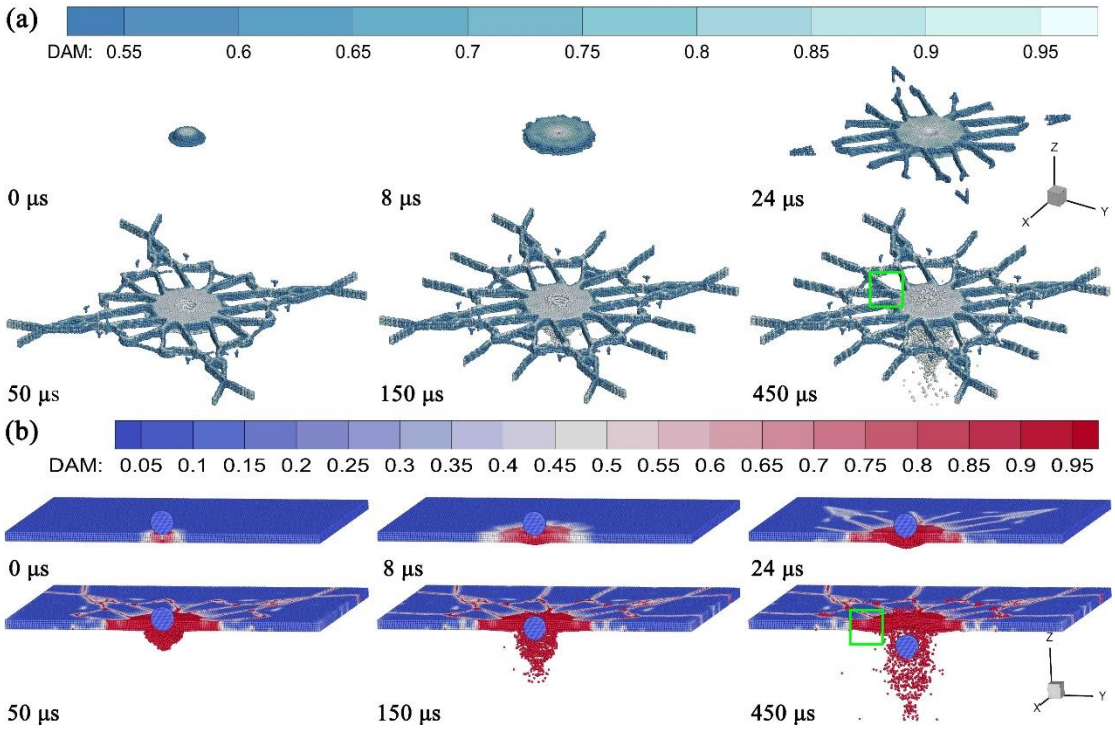

Fig. 15. Damage processes in the thickness direction of the 6-mm-thick ice plate at an impact velocity of 70.8 m/s: (a) the individual fracture surface, and (b) the cross section. Green rectangular symbols indicate the radial crack initiation zone.

3.2.2 Ice breaking of medium ice plates

Fig. 16 shows the failure process of the 10-mm-thick ice plate at an impact velocity of 27.9 m/s. The magnitude of the residual velocity is slightly different from the

experimental tests: the model gives a residual speed of 16.1 m/s, while in the experiments, the measured value is 12.9 m/s (Zhang et al., 2023b). At 50 μs, substantial clustered microcracks appear at the centre of the strike surface (Fig. 16a). At 200 μs, the propagation of 8 radial cracks on the impact surface and back surface are basically synchronized, indicating that these radial cracks are penetrating cracks. At 450 μs, the radial cracks fully extend to the boundary. The area of the debris cloud is larger in the numerical simulation than in the experimental results (Fig. 16d) on the back surface, while the overall crack propagation modes (Figs. 16a and c) are consistent (Zhang et al., 2023b).

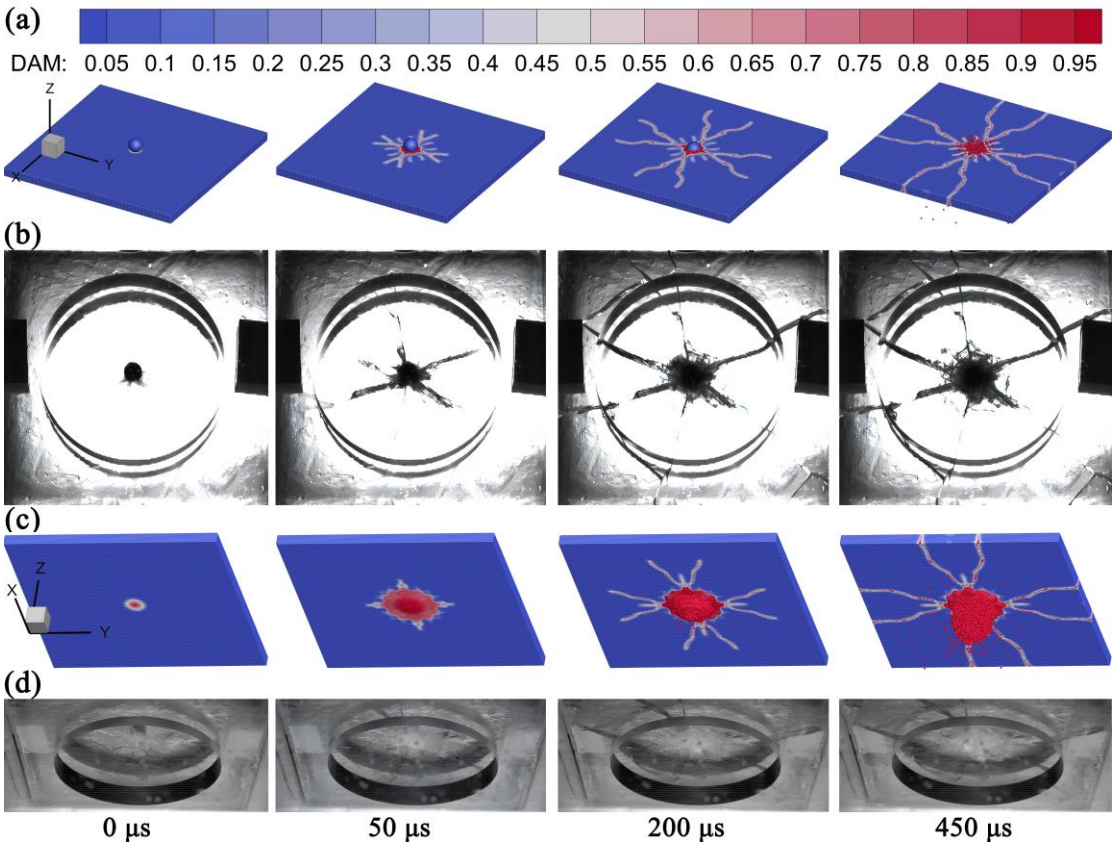

Fig. 16. Comparison of the failure processes of the 10-mm-thick ice plate at an impact velocity of 27.9 m/s: (a) and (c) PD models, and (b) and (d) experimental observations (Zhang et al., 2023b); (a)–(b) strike surfaces, and (c)–(d) back surfaces.

Fig. 17 shows the damage processes in the thickness direction of the 10-mm-thick ice plate at an impact velocity of 27.9 m/s. In Fig. 17a, at contact, a small truncated conical shape damage area is generated. At 12 μs, the crater gradually transforms into a low cone; at 50 μs, the upper conical crater forms; from 100 to 450 μs, the crater shape remains invariant, while 8 radial cracks propagate outwards. Specifically, from 100 to 200 μs, radial cracks propagate not only from the centre to the boundary but also from the strike surface along the thickness to the back surface, which is obviously difficult to observe in tests. At 450 μs, the shape of the upper crater on the 10 mm ice plate is more pronounced than that on the 6 mm ice plate from the cross-sectional view (Fig. 17b), but the diameter of the upper crater is less than that of the lower crater.

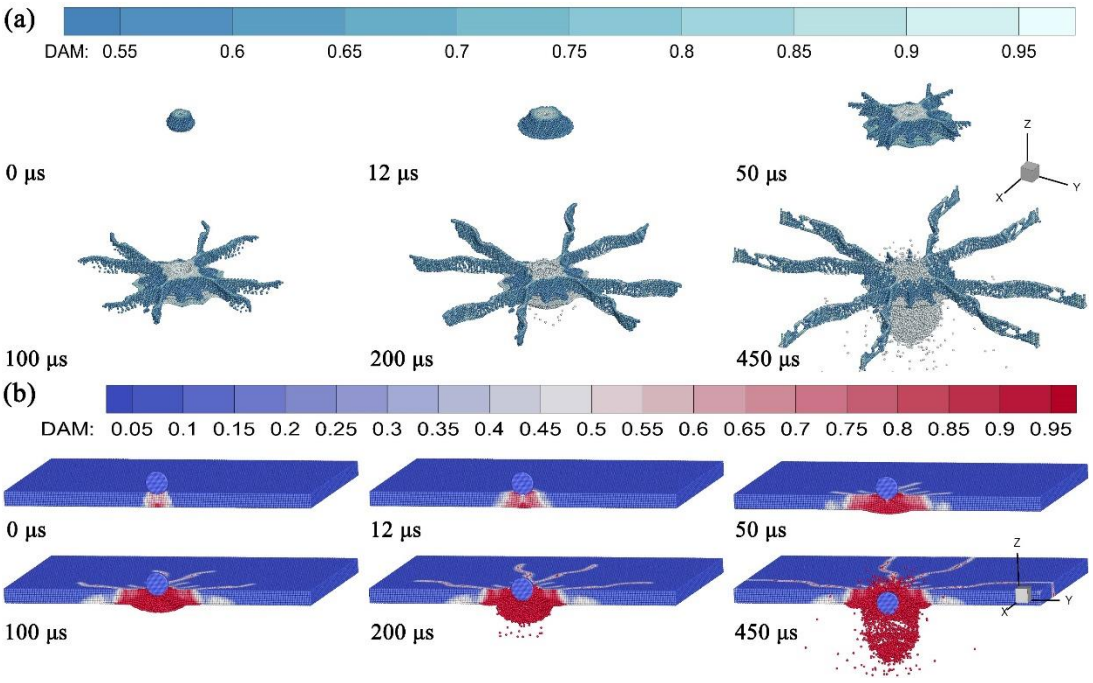

Fig. 17. Damage processes in the thickness direction of the 10-mm-thick ice plate at an impact velocity of 27.9 m/s: (a) the individual fracture surface, and (b) the cross section.

Fig. 18 shows the failure processes of the 10-mm-thick ice plate at an impact velocity of 71.7 m/s. The residual velocity calculated using this PD method agrees well

with the results of physical experiments (Zhang et al., 2023b). The model gives a residual speed of 62.6 m/s, and the value measured in experiments was 60.8 m/s. In Fig. 18a, circumferential cracks continue to form in the ice place at 200 μs, and many radial cracks, branching cracks, and corner cracks are generated instantly, which is consistent with the experimental results (Fig. 18b). In Fig. 18c, the fragmented zone in front of the projectile changes from slightly convex to a semi-ellipsoidal cylinder, which is basically the same as the experimental findings on the back surface (Fig. 18d).

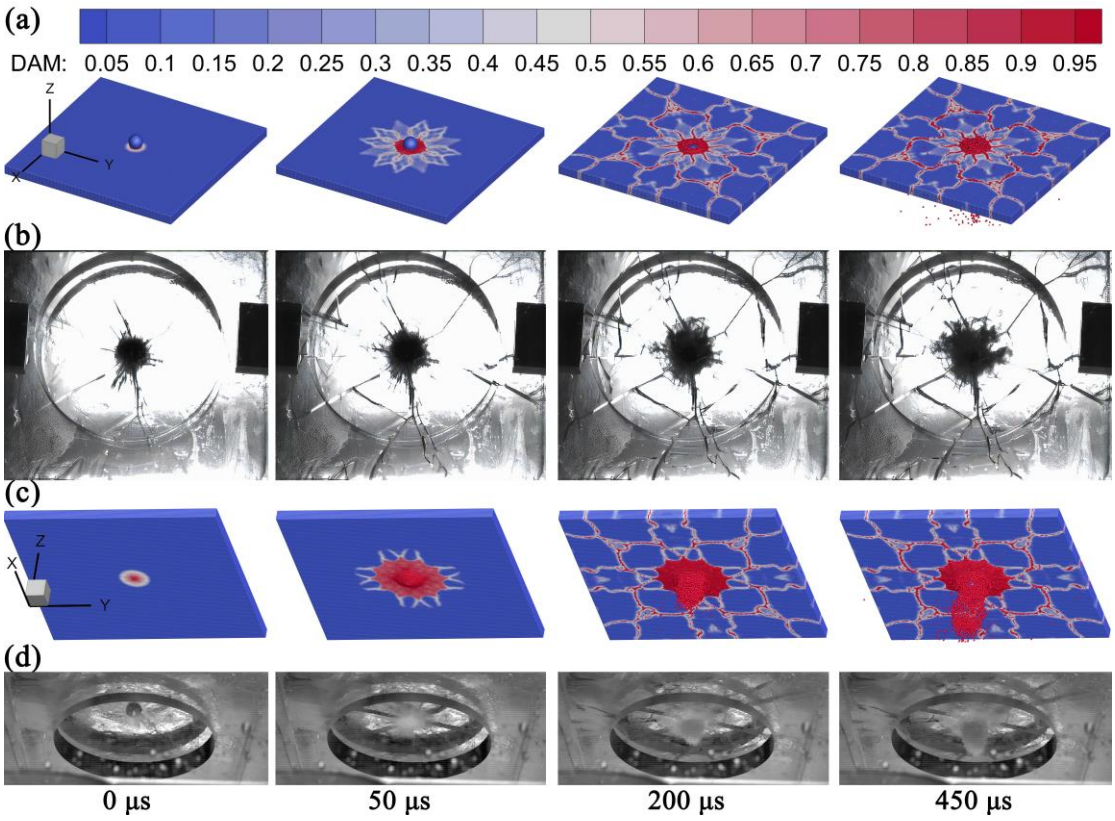

Fig. 18. Comparison of the failure processes of the 10-mm-thick ice plate at an impact velocity of 71.7 m/s: (a) and (c) PD models, and (b) and (d) experimental observations (Zhang et al., 2023b). (a)–(b) strike surfaces, and (c)–(d) back surfaces.

Fig. 19a shows individual images of the damage progression of the 10-mm-thick

ice plate at an impact velocity of 71.7 m/s. At contact, small truncated conical damage occurs; at 12 μs, the high-pressure zone evolves into two short conical craters, and more through-thickness radial cracks at 50 μs initiate from the crater boundary. At 100 μs, the radial crack at the centre appears in the form of a wagon wheel with 8 spokes. At 450 μs, the central red conical damage area in the thickness direction (Fig. 19b) is significantly larger than that at an impact velocity of 28.8 m/s (Fig. 17b).

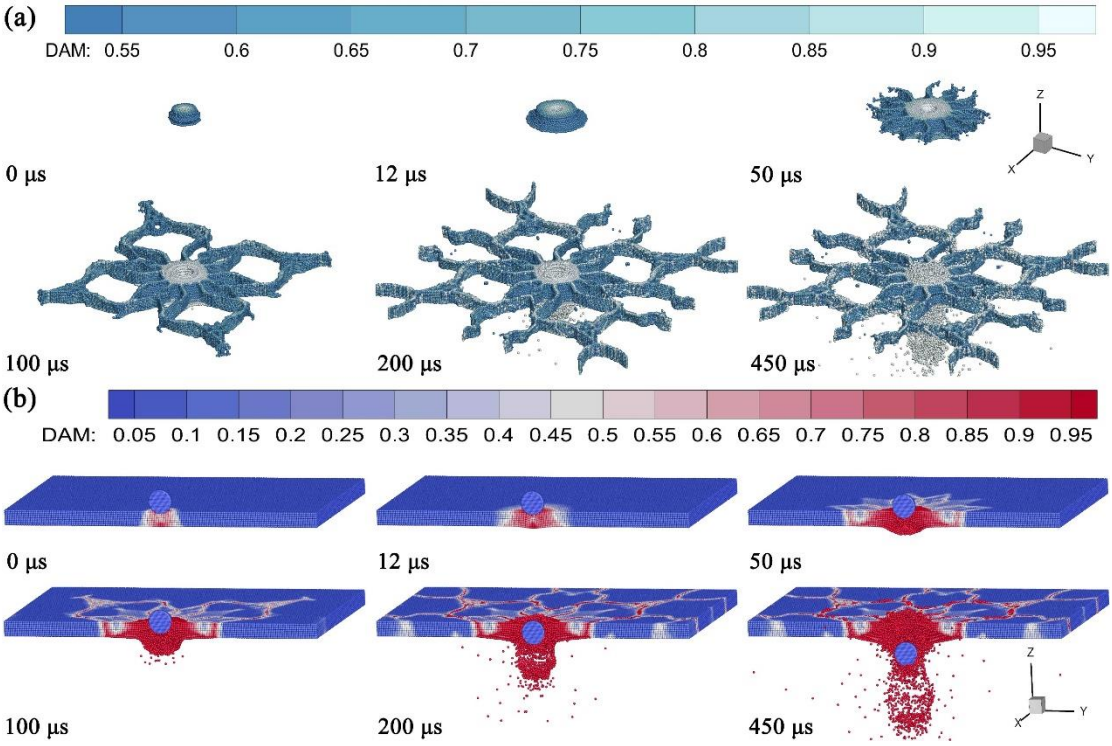

Fig. 19. Damage processes in the thickness direction of the 10-mm-thick ice plate at an impact velocity of 71.7 m/s: (a) the individual fracture surface, and (b) the cross section.

3.2.3 Ice breaking of thick ice plates

Fig. 20 shows the failure processes of a 26-mm-thick ice plate at an impact velocity of 26.3 m/s. The numerically determined residual velocity is 0.8 m/s, which is slightly

less than 2.9 m/s measured in the experiment (Zhang et al., 2023b). The value reveals that the impact velocity is close to the ballistic limit velocity, that is, the projectile just penetrates the ice plate, and the energy is almost completely absorbed by the ice plate, leading to the formation of cracks. In Fig. 20a, four radial cracks at 150 μs start to initiate and propagate near the high-pressure zone; at 1000 μs, the radial cracks propagate to the boundary. The overall numerical simulation results are slightly delayed compared to the fracture process observed in the experiment (Fig. 20b). Unlike the 6- and 10-mm-thick ice plates, no damage appears on the back plate at contact (Fig. 20c). Radial cracks on the back surface at 150 μs evolve slightly faster than those on the impact surface. At 1000 μs, the numerical results show blocks of spalling on the back surface, which is consistent with experimental observations (Fig. 20d).

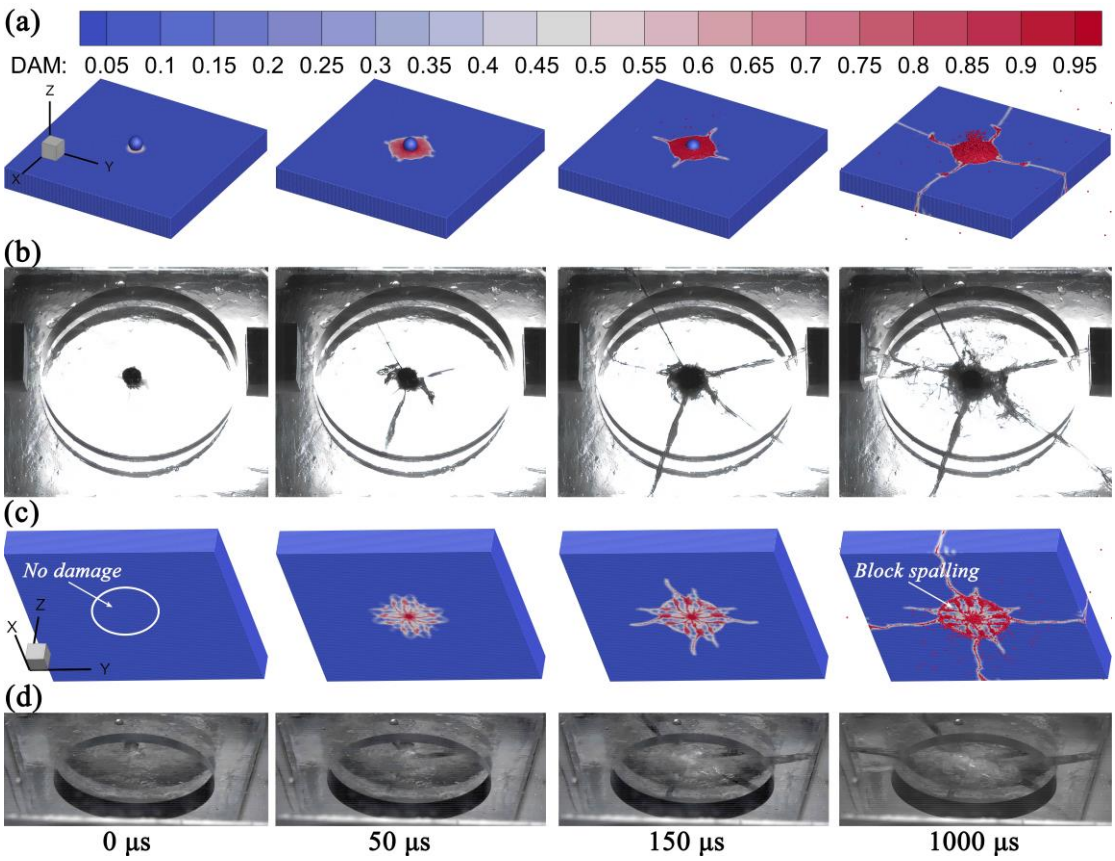

Fig. 20. Comparison of the failure processes of the 26-mm-thick ice plate at an impact velocity of 26.3 m/s: (a) and (c) PD models, and (b) and (d) experimental observations (Zhang et al., 2023b); (a)–(b) strike surfaces, and (c)–(d) back surfaces.

Fig. 21a shows that a small cylinder forms in the local high-pressure zone in the area of contact and then evolves into two stacked cones at 12 μs. The damaged area expands rapidly at 50 μs, and its surface morphology resembles the roots extending from the trunk of a sturdy tree. After 150 μs, radial cracks propagate towards the boundary but also extend from the bottom to the top along the thickness direction for thick ice plates, which is opposite to the radial path of crack propagation in medium-thick ice plates. From the cross-sectional view (Fig. 21b), the shapes of the upper and lower conical craters are visible at 50 μs, and the diameter of the upper crater appears to be less than that of the lower crater. Two forked radial cracks appear near the centre

of the cross section at 150 μs, and they converge with the main radial cracks extending from the rear at 1000 μs.

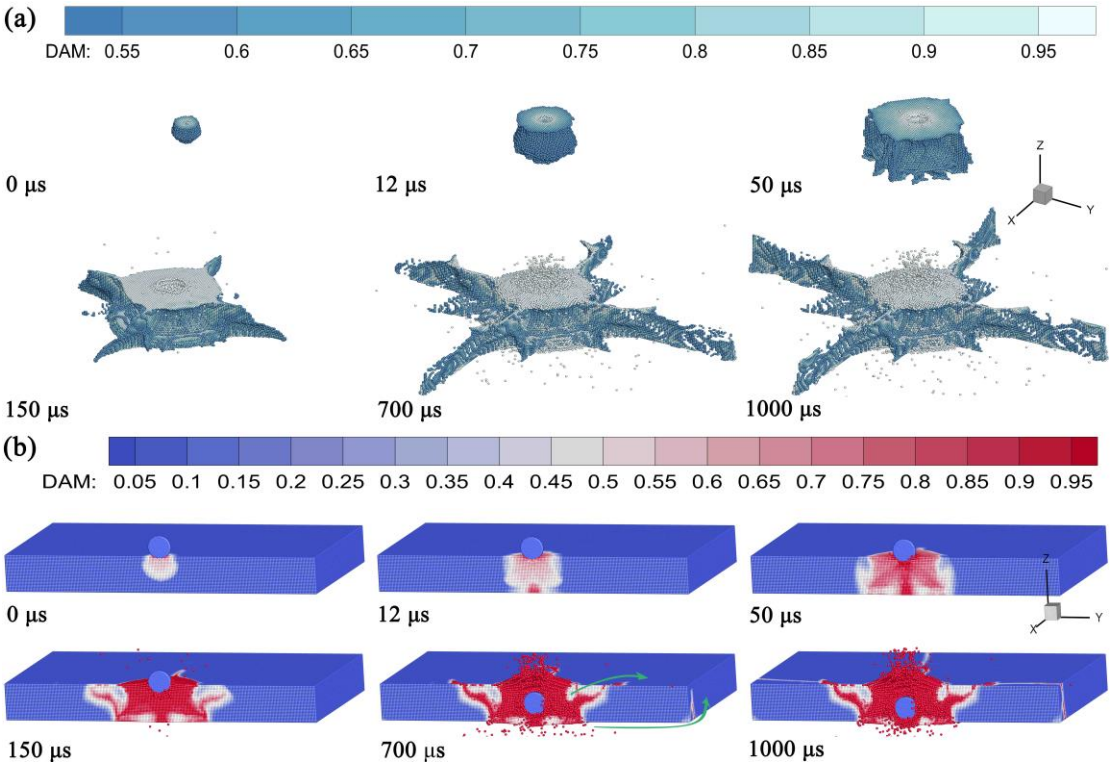

Fig. 21. Damage processes in the thickness direction of the 26-mm-thick ice plate at an impact velocity of 26.3 m/s: (a) the individual fracture surface, and (b) the cross section. Green arrows indicate the propagation direction of radial cracks.

As the impact velocity increases to 72.1 m/s, the PD simulation results on the strike surface (Fig. 22a) show the formation of 8 radial cracks and the appearance of small branched cracks near the fixture opening. Many aggregated broken particles surge upwards in the shape of a head of garlic. The radial crack propagation speed computed by the PD model is slower than the experimental results (Fig. 22b), but the overall evolution trends are highly consistent. At 150 μs, an area of white clusters observed on the bottom surface (Fig. 22d), and the numerical results (Fig. 22c) reveal that it consists of completely fragmented particles that do not scatter in front of the rigid ball.

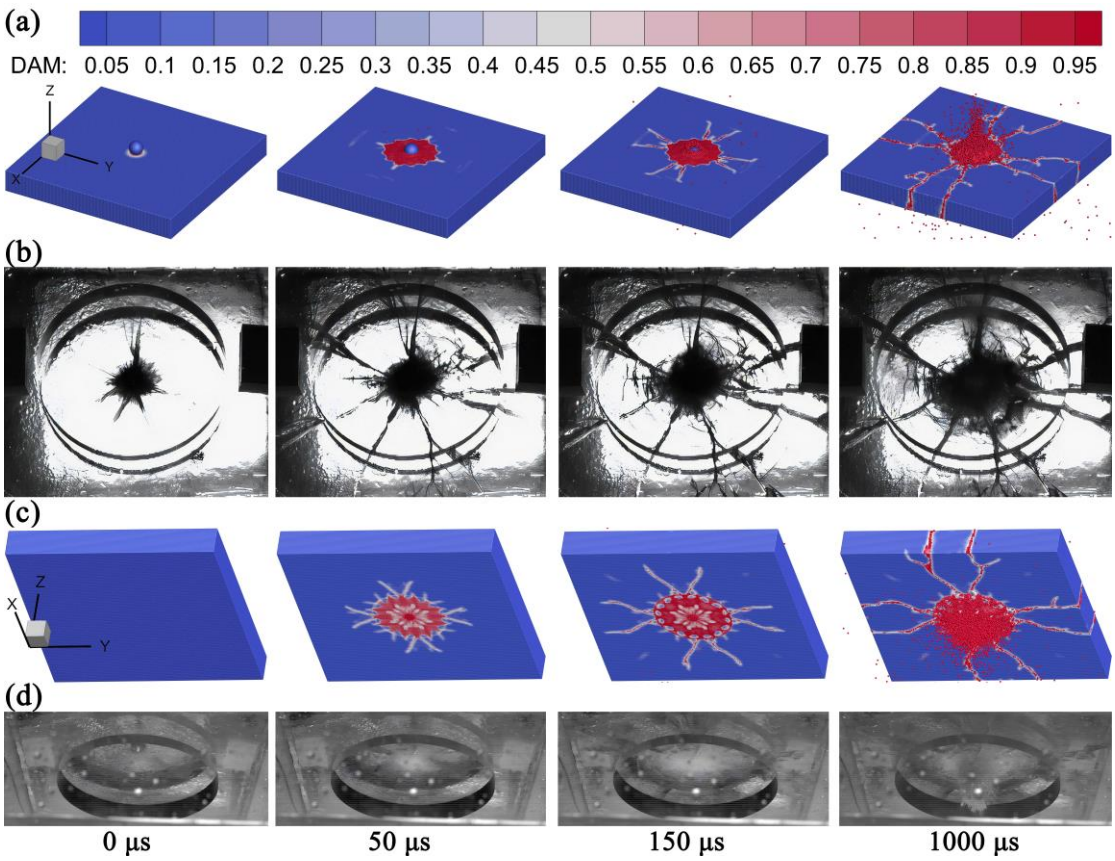

Fig. 22. Comparison of the failure processes of the 26-mm-thick ice plate at an impact velocity of 72.1 m/s: (a) and (c) PD models, and (b) and (d) experimental observations (Zhang et al., 2023b); (a)–(b) strike surfaces, and (c)–(d) back surfaces.

Fig. 23a shows individual images of the damage progression of a 26-mm-thick ice plate at an impact velocity of 72.1 m/s. From 150 to 1000 μs, radial cracks have identical propagation modes, extending from the back plate to the strike surface while propagating towards the boundary. In the cross-sectional view, the diameter of the upper crater is still slightly less than that of the lower crater at 50 μs, and the crater shape remains basically unchanged thereafter, as shown in Fig. 23b.

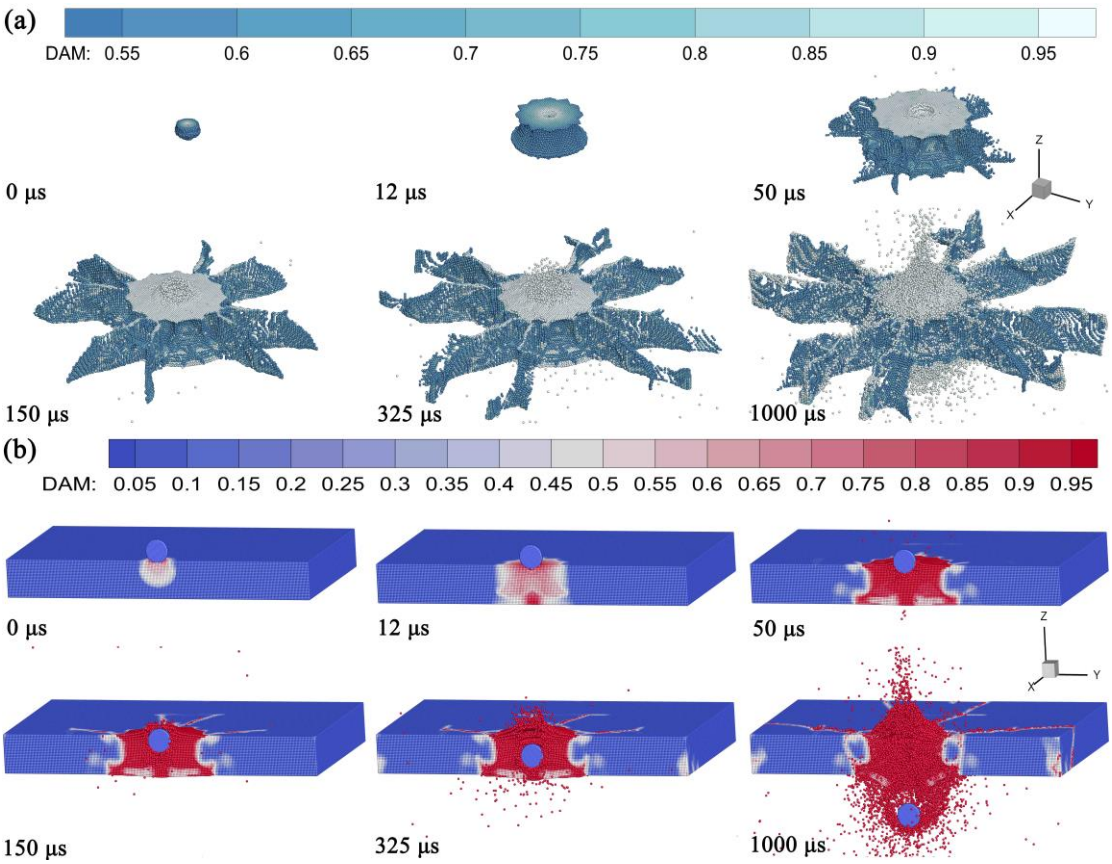

Fig. 23. Damage processes in the thickness direction of the 26-mm-thick ice plate at an impact velocity of 72.1 m/s: (a) the individual fracture surface, and (b) the cross section.

3.3 Factors influencing failure modes

3.3.1 Impact velocity

Fig. 24 shows the damage maps of the 10-mm-thick ice plate computed by the PD simulations at various impact velocities. For the 5 m/s case, the rigid ball does not penetrate the ice plate and only local radial cracks form. As the speed increases to 10 m/s, the projectile is still unable to penetrate the ice plate; however, four straight radial cracks extend from the centre to the edge. At an impact speed of 20 m/s, the projectile just penetrates the ice plate and small particles splash on the impact surface; however,

the final failure mode remains unchanged. For the 27.9 m/s case, the number of radial cracks increases to 8. At an impact speed of 52.9 m/s, local failure increases, and boundary cracks appear. For the 71.7 m/s case, many circumferential cracks occur. At an impact speed of 100 m/s, the ice plate breaks more severely. From 150 to 200 m/s impact speed, the size of the completely comminuted area (dark red concentrated zone in Fig. 24) in the centre rapidly increases. A network of dense cracks develops near the boundary as the speed reaches 200 m/s, and the debris clouds on the strike surface centre resemble a surging wave in a body of water.

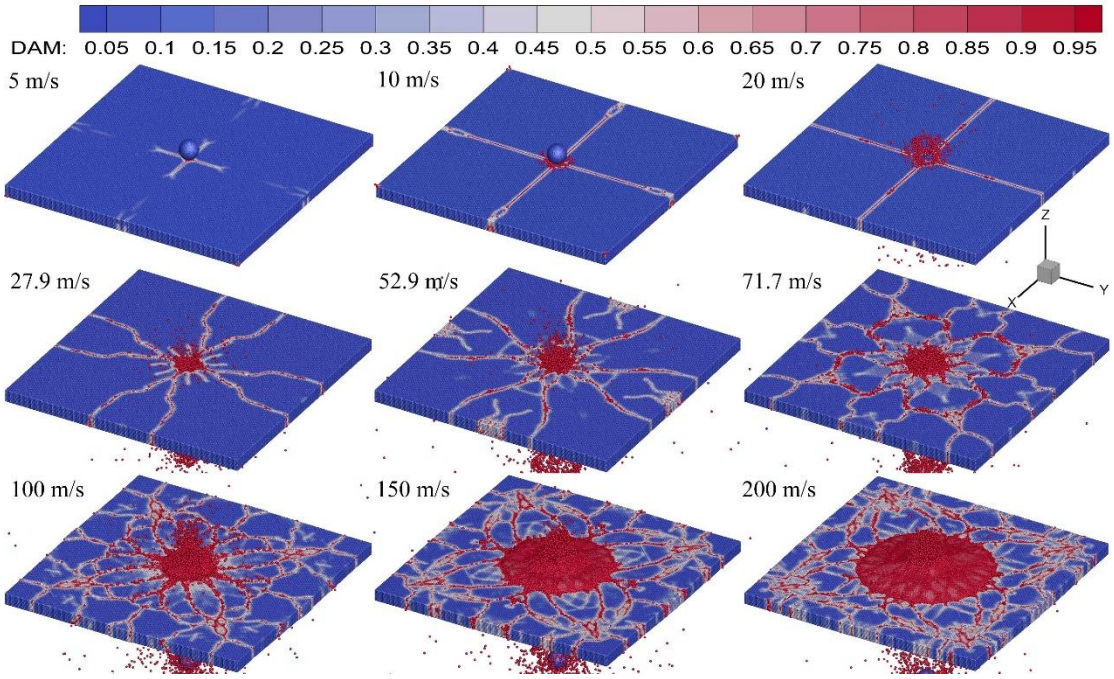

Fig. 24. Damage of the 10-mm-thick ice plate obtained by the PD model at different impact velocities.

3.3.2 Ice thickness

In the test, the speed of the bullet is indirectly controlled by adjusting the pressure

of an air gun. Therefore, tiny deviations in the bullet speed at the same air pressure may lead to experimental errors. In addition, ice plates with thicknesses less than 5 mm are fragile during handling and clamping, and it is difficult to prepare ice plates with thicknesses more than 50 mm with no visible bubbles. Consequently, this section compares and analyses the failure progression of ice plates computed by PD within a large thickness range at the same impact velocity.

To better observe the crater surface morphology, we remove the completely damaged particles (D =1). Fig. 25 shows the formation of craters on the cross sections of ice plates with different thicknesses at typical moments. There is no significant difference in the local failure process between the 4-mm- and 6-mm-thick ice plates. In both cases, complete circumferential cracks form, and the central area of local damage resembles a smooth crater perpendicular to the surface of the ice plate. The crater diameter decreases slightly as the ice thickness increases. Notably, from 80 to 550 μs, circumferential cracks in the 6-mm-thick ice plates propagate from a radial crack to an adjacent radial crack rather than initiating and converging in tandem from two adjacent radial cracks. For the 10-mm-thick ice plates, a clear conical crater forms at 132 μs; a smooth crater surface and slices of spalling fragments appear at 840 μs. For the 26-mm-thick ice plates, the circumferential crack disappears. The upper conical crater is more apparent, and the crater surface is rougher. The diameter of the upper crater is close to that of the lower crater. At 550 μs, a large amount of peeling occurs at the bottom. At 1300 μs, because the velocity of the projectile is greater than that of the peeled block, the block shatters into multiple scattered blocks.

The 60-mm-thick ice target can be regarded as an ice block, and its failure mode is entirely distinct from those of ice plates with thicknesses of 4–26 mm. At 800 μs, the ice target no longer has radial cracks, and only a conical upper crater forms. At 1600 μs, a rigid ball penetrates through the ice block. A cylindrical tunnelling zone forms in the centre of the cross section, and a deeper conical crater with a small amount of peeling is produced at the end of the trajectory. The steep surface can be clearly seen on the upper conical crater, further confirming the speculation in a paper about an experiment from the literature (Zhang et al., 2023b). Under the same impact velocity, for the thin and medium ice plates, kinetic energy is distributed to initiate radial and circumferential micro-cracks along the thickness direction, and complete local fragmentation tends to produce a smooth surface. However, for thick ice targets, more energy is transferred to break ice along the thickness direction, and local nonviolent damage ultimately forms rough and uneven surfaces.

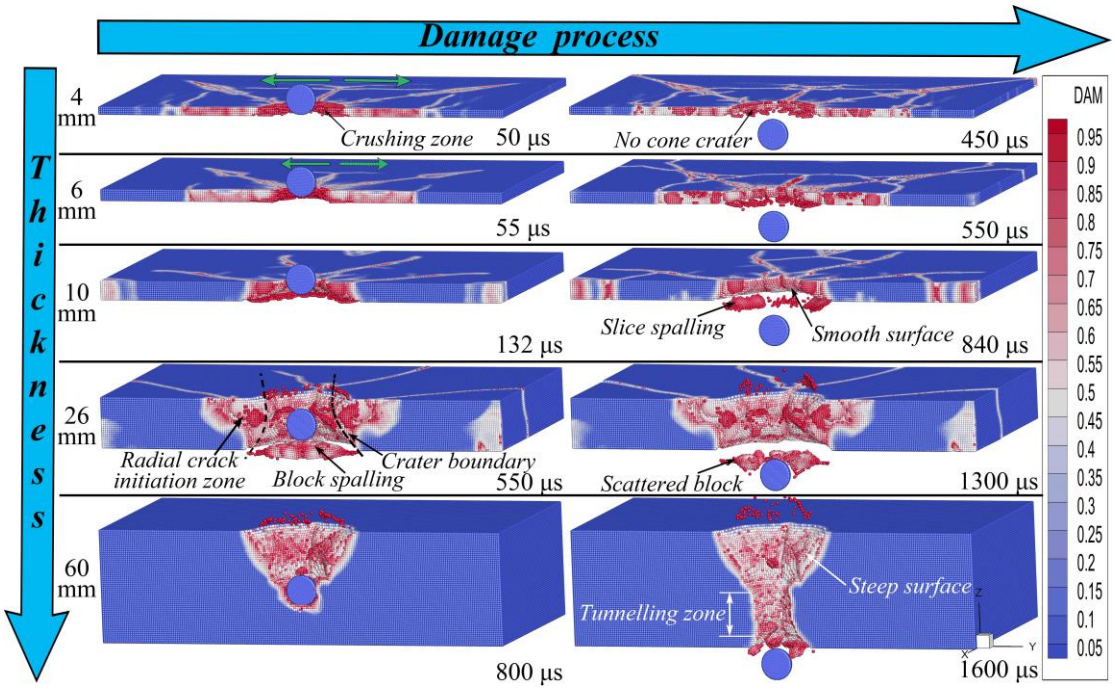

Fig. 25. Typical cross-sectional views of the processes of crater formation in ice plates

with various thicknesses at an impact velocity of 50 m/s. Green arrows indicate the propagation direction of circumferential cracks.

3.3.3 Boundary constraint conditions

To explore the influence of boundary constraints (with or without fixed upper and lower surface conditions) on the failure modes of ice plates, two representative examples are selected. Figs. 26a–b show the failure results of a 10-mm-thick ice plate with upper and lower fixed constraints and only lower fixed constraints, respectively. The upper fixed constraint has little effect on the failure results, which is consistent with the conclusions drawn from the experimental results (Figs. 26d–e). Fig. 26c shows that the lower fixed constraint still has no significant effect on the final failure mode in this case. The study indicates that the deflection of the ice plate is slight during the transient impact, and the subsequent vibration no longer causes additional crack propagation.

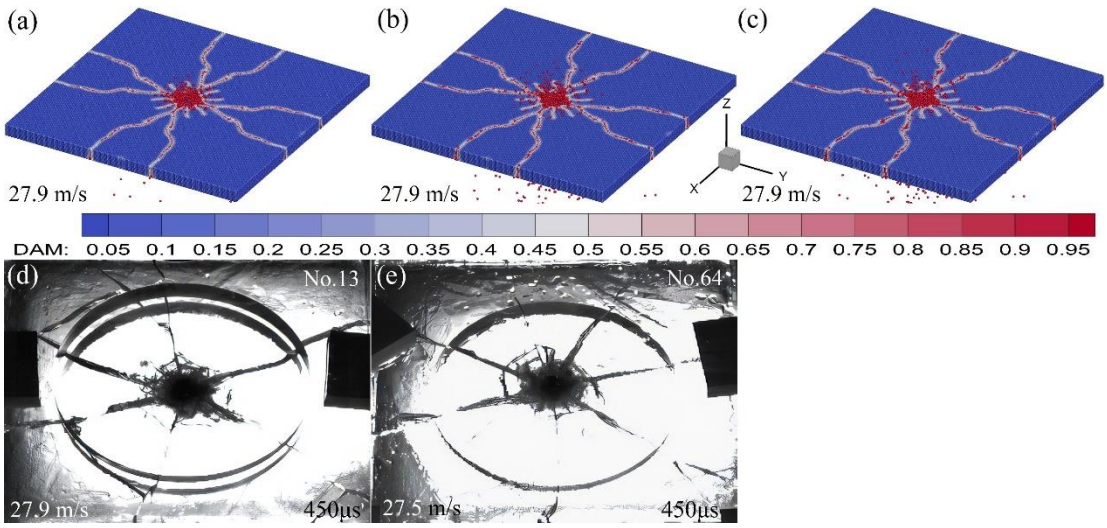

Fig. 26. Failure results for a 10-mm-thick ice plate with different restrictions at similar impact velocities: (a)–(c) are the PD simulation results with upper and lower fixed

constraints, only a lower fixed constraint, and no upper and lower constraints, respectively; and (d)–(e) are the experimental observations with upper and lower fixed constraints and only a lower fixed constraint, respectively (Zhang et al., 2023b).

Fig. 27a shows the failure results of a 6-mm-thick ice plate with different restrictions at an impact velocity of 70.8 m/s. The central circumferential crack zone reflects the effect of constraint by the upper and lower fixtures with openings. With only a lower constraint (Fig. 27b), more microcracks appear on the impact surface. However, without any constraints, the circumferential cracks at the centre exhibit more severe damage, and the range of the circumferential cracks is greater than the opening diameter (15 mm). Therefore, if circumferential cracks appear on an ice plate, the presence of the lower fixed constraint has a significant effect on failure.

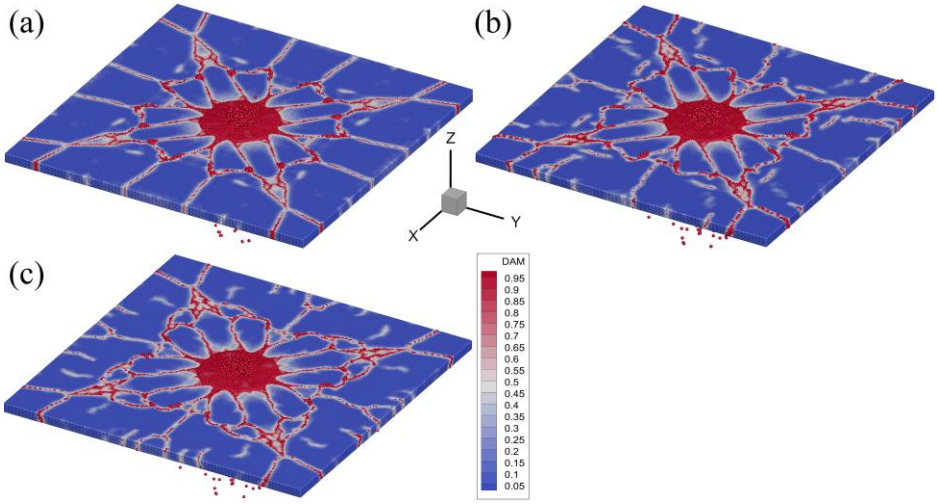

Fig. 27. Numerical failure results of a 6-mm-thick ice plate at an impact velocity of 70.8 m/s with different restrictions: (a) upper and lower fixed constraints, (b) only a lower fixed constraint, and (c) no upper and lower fixed constraints.

4. Conclusions

This paper presents the results of numerical simulations of the damage of ice plates subject to impacts by small spherical projectiles at various impact velocities. The proposed 3D rate-dependent peridynamics model is validated by comparison with experimental results from the dynamic ring Brazilian disc ice test. The dynamic fracture processes of the ice plates upon impact by a rigid ball are compared and analysed with previous experimental results, and the factors influencing the modes of failure are explored. The following conclusions are drawn from the results:

For simplified boundary conditions, the virtual boundary layer method produces apparent local circular damage at the opening of the acrylic frame, while the fixed rigid contact model effectively reduces this effect and improves the calculation efficiency. Compared with peridynamics model accounting for the tensile strength rate effect, the proposed model accounting for the fracture toughness rate effect is more suitable for simulating crack propagation in ice plates under impact loading.

Good agreement is found between the proposed model and previous experiments in terms of ice breaking processes of thin, medium and thick ice plates. For thin ice plates, radial and circumferential cracks appear in the numerical model, and the surrounding area of the lower conical crater gradually crumbles after contact. Circumferential cracks present a petal-like form, and two circumferential cracks are observed with increasing impact velocity. For the medium-thick ice plates, circumferential cracks no longer appear at low impact velocities, and an upper conical crater forms. The ice plate recovers to produce circumferential cracks with increasing impact velocity. For thick ice plates, circumferential cracks completely disappear, and

the number of radial cracks decreases. At lower impact velocities, block spalling occurs at the bottom of the ice plate. As the impact velocity increases, damage on the back face becomes extensive and diffuse, with the debris on the strike surface resembling the shape of a head of garlic.

The calculation results reveal detailed characteristics of cracks that were not observed in experiments, such as the sequence and shape of propagating cracks during shorter time intervals and crater formation and damage evolution along the thickness direction. For thin or medium thickness ice plates, cracks basically penetrate and propagate towards the boundary of the ice plate. Partial nonpenetrating radial cracks extend from the top to the bottom. For thick ice plates, radial cracks tend to extend towards the boundary and grow along the thickness direction from the back to the top. Circumferential cracks sometimes initiate and converge simultaneously from two adjacent radial cracks, while sometimes they propagate from a radial crack to an adjacent radial crack. No spalling cracks produced by the reflected tensile wave preferentially appear on the rear after contact. In cross-sectional views, the damage always initiates and expands rapidly from the high-pressure zone to the bottom along the thickness.

For medium or thick ice plates where only radial cracks form, the presence of boundary constraints has little effect on the damage mode. However, for thin ice plates that evolve into circumferential cracks, the constraint of the upper surface still has no obvious effect. However, the presence of the lower boundary constraint with an opening has a significant effect on suppressing the range of circumferential cracks.

For the same ice thickness, as the impact velocity increases, the final failure modes of the ice plates change from no perforation accompanied by several nonpenetrating radial cracks to a network of radial and circumferential cracks. Branching cracks, corner cracks, and boundary cracks gradually appear and rapidly increase in size. When the impact speed is greater than 150 m/s, massive catastrophic damage appears at the centre, forming in a pattern that resembles a surging wave in a body of water.

For the same impact velocity, as the ice thickness increases, the numerical results further confirm the mechanism of the transition of the crater surfaces from smooth to steep. For the thick ice plates, the same kinetic energy preferentially causes penetration damage along the thickness direction rather than further damage on the crater surface or initiating more radial cracks near the high-pressure zone, ultimately generating a rougher upper crater surface. Moreover, the studies reveal great differences in the damage process, crater shape, and failure mechanism between the 60-mm-thick ice target and the 4–26-mm-thick ice plates, demonstrating the potential of the present peridynamics model for simulating projectile penetration into thick ice blocks.

Compared to the top and bottom views, the cross-sectional view is more useful for observing the movement of the projectile and the formation of debris clouds, but it is not suitable for determining the crater diameter, especially in cases with complex failure modes. The crater boundary of the transverse section may form a radial crack initiation zone, which interferes with the determination of the actual crater shape and size.

The impact speed of the projectile is aimed at the low-speed impact range in current study. Therefore, ice is simply regarded as an elastic brittle material. However,

as the impact velocity increases from 100 m/s to tens of km/s, thermo-mechanical effect gradually emerges. Ice material presents a sophisticated failure mechanism transition from viscoelastic plasticity (Pernas-Sánchez et al, 2012) to melting and vaporization (Stewart et al, 2008) characteristics. The simulation results of the local damage area are generally larger than the experimental results, which may be related to the plastic deformations of the rigid ball and the ice plate during the initial stage of impact. Therefore, we conduct only qualitative analysis on the crater parameters. It is meaningful to establish an elastic–plastic constitutive model suitable for ice in the state-based peridynamics model that will more accurately characterize the progression of damage and reveal the fracturing mechanism in penetrator–ice impact tests.

Acknowledgements

This work was supported by the National Natural Science Foundation of China (NSFC) [Grant Nos. 52192690；52192695].

References

Anicode, V., Diyaroglu, C., Madenci, E., 2020. Peridynamic modeling of dama ge due to multiple sand particle impacts in the presence of contact and fri ction, AIAA Scitech 2020 Forum, p. 0968. https://doi.org/10.2514/6.2020-09 68

Arakawa, M., Shirai, K., Kato, M., 2000. Shock wave and fracture propagation in water ice by high velocity impact. Geophys. Res. Lett. 27 (3), 305-30

8. https://doi.org/10.1029/1999GL010841

Barash, R.M., 1966. Ice-breaking by explosives. Naval Ordnance Lab White Oa k Md.

Bayer, T., Cooke, B., Gontijo, I., Kirby, K., 2015. Europa Clipper mission: the habitability of an icy moon, 2015 IEEE Aerospace Conference. IEEE, pp. 1-12. https://doi.org/10.1109/AERO.2015.7118943

Bobaru, F., Ha, Y.D., Hu, W., 2012. Damage progression from impact in layer ed glass modeled with peridynamics. Cent. European J. Eng. 2, 551-561. h ttps://doi.org/10.2478/s13531-012-0020-6

Chu, B., Liu, Q., Liu, L., Lai, X., Mei, H., 2020. A rate-dependent peridynami c model for the dynamic behavior of ceramic materials. Comp. Model. En g. 124 (1), 151-178. https://doi.org/10.32604/cmes.2020.010115

Fan, H., Bergel, G.L., Li, S., 2016. A hybrid peridynamics–SPH simulation of soil fragmentation by blast loads of buried explosive. Int. J. Impact Eng. 87, 14-27. https://doi.org/10.1016/j.ijimpeng.2015.08.006

Fan, J., Xie, H., Li, S., Zhang, H., Zhang, Y., 2023. New insights into the bo nd-based and ordinary state-based models in Peridynamics. Eng. Fract. Me ch. 277, 108991. https://doi.org/10.1016/j.engfracmech.2022.108991

Gu, X., Zhang, Q., Huang, D., Yv, Y., 2016. Wave dispersion analysis and sim ulation method for concrete SHPB test in peridynamics. Eng. Fract. Mech. 160, 124-137. https://doi.org/10.1016/j.engfracmech.2016.04.005

Ha, Y.D., 2020. An extended ghost interlayer model in peridynamic theory for

high-velocity impact fracture of laminated glass structures. Comput. Math. Appl. 80 (5), 744-761. https://doi.org/10.1016/j.camwa.2020.05.003

Ha, Y.D., Bobaru, F., 2010. Studies of dynamic crack propagation and crack br anching with peridynamics. Int. J. Fract. 162, 229-244. https://doi.org/10.10 07/s10704-010-9442-4

Han, D.F., Zhang, Y.H., Wang, Q., Lu, W., Jia, B., 2019. The review of the b ond-based peridynamics modeling. J. Micromech. Mol. Phys. 4 (01), 18300 01. https://doi.org/10.1142/S2424913018300013

Hu, W., Wang, Y., Yu, J., Yen, C.F., Bobaru, F., 2013. Impact damage on a th in glass plate with a thin polycarbonate backing. Int. J. Impact Eng. 62, 1 52-165. https://doi.org/10.1016/j.ijimpeng.2013.07.001

Iijima, Y.i., Kato, M., Arakawa, M., Maeno, N., Fujimura, A., Mizutani, H., 19 95. Cratering experiments on ice: Dependence of crater formation on proje ctile materials and scaling parameter. Geophys. Res. Lett. 22 (15), 2005-20 08. https://doi.org/10.1029/95GL01894

Javili, A., Morasata, R., Oterkus, E., Oterkus, S., 2019. Peridynamics review. Math. Mech. Solids 24 (11), 3714-3739. https://doi.org/10.1177/1081286518 803411

Jou, O., Celigueta, M.A., Latorre, S., Arrufat, F., Oñate, E., 2019. A bonded d iscrete element method for modeling ship–ice interactions in broken and u nbroken sea ice fields. Comput. Part. Mech. 6 (4), 739-765.https://doi.org/1 0.1007/s40571-019-00259-8

Kan, X.Y., Zhang, A.M., Yan, J.L., Wu, W.B., Liu, Y.L., 2020. Numerical investigation of ice breaking by a high-pressure bubble based on a coupled BEM-PD model. J. Fluid. Struct. 96, 103016. https://doi.org/10.1016/j.jfluidstructs.2020.103016

Kato, M., Iijima, Y.I., Arakawa, M., Okimura, Y., Fujimura, A., Maeno, N., Mizutani, H., 1995. Ice-on-ice impact experiments. Icarus 113 (2), 423-441. https://doi.org/10.1006/icar.1995.1032

Kim, M.C., Lee, S.K., Lee, W.J., Wang, J., 2013. Numerical and experimental investigation of the resistance performance of an icebreaking cargo ship in pack ice conditions. Int. J. Naval Architect. Ocean Eng. 5 (1), 116–131. https://doi.org/10.3744/JNAOE.2013.5.1.116

Kim, M.C., Lee, W.J., Shin, Y.J., 2014. Comparative study on the resistance performance of an icebreaking cargo ship according to the variation of water line angles in pack ice conditions. Int. J. Naval Architect. Ocean Eng. 6, 876–893. https://doi.org/10.2478/ijnaoe-2013-0219

Lange, M.A., Ahrens, T.J., 1987. Impact experiments in low-temperature ice. Icarus 69 (3), 506-518. https://doi.org/10.1016/0019-1035(87)90020-0

Lee, S.G., Zhao, T., Kim, G.S., Park, K.D., 2013. Ice resistance test simulation of arctic cargo ship using FSI analysis method. In: Proc. Of the 23rd International Offshore and Polar Engineering Conference, ISOPE 2013, pp. 1162–1168

Leslie, D.M., Nelson, C.A., 1961. Explosion tests under thick polar ice. Naval

Ordnance Lab White Oak Md.

Levine, J.A., Bargteil, A.W., Corsi, C., Tessendorf, J., Geist, R., 2014. A Peridynamic Perspective on Spring-Mass Fracture, Symposium on Computer Animation, pp. 47-55. http://dx.doi.org/10.2312/sca.20141122

Li, J.B., Wang, C.Y., Wang, Q., Zhang, Y.H., Jing, C.Y., Han, D.F., 2023. Peridynamic modeling of polycrystalline S2 ice and its applications. Eng. Fract. Mech. 277, 108941. https://doi.org/10.1016/j.engfracmech.2022.108941

Li, J.B., Wang, Q., Li, X.F., Ju, L., Zhang, Y.H., 2022. Homogenization of periodic microstructure based on representative volume element using improved bond-based peridynamics. Eng. Anal. Bound. Elem. 143, 152-162. https://doi.org/10.1016/j.enganabound.2022.06.005

Li, P., Hao, Z., Zhen, W., 2018. A stabilized non-ordinary state-based peridynamic model. Comput. Method. Appl. M. 339, 262-280. https://doi.org/10.1016/j.cma.2018.05.002

Liu, M., Wang, Q., Lu, W., 2017. Peridynamic simulation of brittle-ice crushed by a vertical structure. Int. J. Nav. Arch. Ocean 9 (2), 209-218. https://doi.org/10.1016/j.ijnaoe.2016.10.003

Liu, R.W., Xue, Y.Z., Lu, X.K., Cheng, W.X., 2018. Simulation of ship navigation in ice rubble based on peridynamics. Ocean Eng. 148, 286-298. https://doi.org/10.1016/j.oceaneng.2017.11.034

Liu, R.W., Yan, J.L., Li, S.F., 2020a. Modeling and simulation of ice–water interactions by coupling peridynamics with updated Lagrangian particle hydro

dynamics. Comput. Part. Mech. 7, 241-255. https://doi.org/10.1007/s40571-019-00268-7

Liu, S., Fang, G., Fu, M., Yan, X., Meng, S., Liang, J., 2022a. A coupling model of element-based peridynamics and finite element method for elastic-plastic deformation and fracture analysis. Int. J. Mech. Sci. 220, 107170. https://doi.org/10.1016/j.ijmecsci.2022.107170

Liu, S., Fang, G., Liang, J., Lv, D., 2020b. A coupling model of XFEM/peridynamics for 2D dynamic crack propagation and branching problems. Theor. Appl. Fract. Mec. 108, 102573. https://doi.org/10.1016/j.tafmec.2020.102573

Liu, Y., Liu, L., Mei, H., Liu, Q., Lai, X., 2022b. A modified rate-dependent peridynamic model with rotation effect for dynamic mechanical behavior of ceramic materials. Comput. Method. Appl. M. 388, 114246. https://doi.org/10.1016/j.cma.2021.114246

Long, X., Liu, S., Ji, S., 2021. Breaking characteristics of ice cover and dynamic ice load on upward-downward conical structure based on DEM simulations. Comput. Part. Mech. 8 (2), 297-313. https://doi.org/10.1007/s40571-020-00331-8

Lu, W., Li, M., Vazic, B., Oterkus, S., Oterkus, E., Wang, Q., 2020. Peridynamic modelling of fracture in polycrystalline ice. J. Mech. 36 (2), 223-234. https://doi.org/10.1017/jmech.2019.61

Ma, P., Li, S., Zhou, H., Zhao, S., Wang, P., Wan, Z., Zhi, B., 2021. Peridynamic method to determine energy absorption characteristics of ordinary glas

s under impact load. Int. J. Crashworthines. 26 (2), 227-235. https://doi.org/10.1080/13588265.2019.1701890

Madenci, E., Oterkus, E., 2013. Peridynamic theory, Peridynamic Theory and Its Applications. Springer, pp. 19-43. https://doi.org/10.1007/978-1-4614-8465-3

Madenci, E., Oterkus, E., 2013. Impact problems. Peridynamic Theory and Its Applications, 181-190. https://doi.org/10.1007/978-1-4614-8465-3

Marusiak, A.G., Vance, S., Panning, M.P., Běhounková, M., Byrne, P.K., Choblet, G., Daswani, M.M., Hughson, K., Journaux, B., Lobo, A.H., 2021. Exploration of icy ocean worlds using geophysical approaches. Planet. Sci. J. 2 (4), 150. https://doi.org/10.3847/PSJ/ac1272

Mellor, M., 1982. Breaking ice with explosives.

Millan, J., Wang, J., 2011. Ice force modelling for DP control system. In: Dynamic Positioning Conference, Houston, Texas, USA, 2011, p. 11p.

Oterkus, E., Guven, I., Madenci, E., 2012. Impact damage assessment by using peridynamic theory. Cent. Eur. J. Eng. 2, 523-531. https://doi.org/10.2478/s13531-012-0025-1

Pernas-Sánchez, J., Pedroche, D.A., Varas, D., López-Puente, J., Zaera, R., 2012. Numerical modeling of ice behavior under high velocity impacts. Int. J. Solids Struct. 49 (14):1919-1927. https://doi.org/10.1016/j.ijsolstr.2012.03.038

Petrovic, J., 2003. Review mechanical properties of ice and snow. J. Mater. Sci. 38, 1-6. https://doi.org/10.1023/A:1021134128038

Rädel, M., Willberg, C., 2018. Peridigm Users Guide. https://elib.dlr.de/126320/1/Peridigm_Users_Guide.pdf

Ren, B., Fan, H., Bergel, G.L., Regueiro, R.A., Lai, X., Li, S.F., 2015. A peri dynamics–SPH coupling approach to simulate soil fragmentation induced by shock waves. Comput. Mech. 55, 287-302. https://doi.org/10.1007/s00466-014-1101-6

Ren, B., Wu, C., Askari, E., 2017. A 3D discontinuous Galerkin finite element method with the bond-based peridynamics model for dynamic brittle failure analysis. Int. J. Impact Eng. 99, 14-25. https://doi.org/10.1016/j.ijimpeng.2016.09.003

Ren, H., Zhao, X., 2022. Numerical simulation for ice breaking and water entry of sphere. Ocean Eng. 243, 110198. https://doi.org/10.1016/j.oceaneng.2021.110198

Silling, S.A., 2000. Reformulation of elasticity theory for discontinuities and long-range forces. J. Mech. Phys. Solids 48 (1), 175-209.

Silling, S.A., Askari, E., 2005. A meshfree method based on the peridynamic model of solid mechanics. Comput. Struct. 83 (17-18), 1526-1535. https://doi.org/10.1016/S0022-5096(99)00029-0

Silling, S.A., Epton, M., Weckner, O., Xu, J., Askari, E., 2007. Peridynamic states and constitutive modeling. J. Elasticity 2 (88), 151-184. https://doi.org/10.1007/s10659-007-9125-1

Silling, S.A., Fermen-Coker, M., 2021. Peridynamic model for microballistic pe

rforation of multilayer graphene. Theor. Appl. Fract. Mec. 113, 102947. https://doi.org/10.1016/j.tafmec.2021.102947

Song, Y., Liu, R.W., Li, S.F., Kang, Z., and Zhang, F., 2020. Peridynamics modeling and simulation of coupled thermomechanical removal of ice from frozen structures. Meccanica. 55, 961-976. https://doi.org/10.1007/s11012-019-01106-z

Song, Y., Li, S.F., Li, Y., 2023. Peridynamic modeling and simulation of thermo-mechanical fracture in inhomogeneous ice. Eng. Comput. 39(1), 575-606. https://doi.org/10.1007/s00366-022-01616-7

Song, Y., Li, S.F., Zhang, S., 2021. Peridynamic modeling and simulation of thermo-mechanical de-icing process with modified ice failure criterion. Def. Technol. 17 (1), 15-35. https://doi.org/10.1016/j.dt.2020.04.001

Song, Y., Yu, H., Kang, Z., 2018. Numerical study on ice fragmentation by impact based on non-ordinary state-based peridynamics. J. Micromech. Mol. Phys. 4 (01), 1850006. https://doi.org/10.1142/S2424913018500066

Song, Y., Yan, J.L., Li, S.F., Kang, Z., 2019. Peridynamic modeling and simulation of ice craters by impact. Comp. Model. Eng. 121(2), 465-492. https://doi.org/10.32604/cmes.2019.07190

Stewart, S.T., Seifter, A., Obst, A.W., 2008. Shocked H_2O ice: Thermal emission measurements and the criteria for phase changes during impact events. Geophys. Res. Lett. 35(23): L23203. https://doi.org/10.1029/2008GL035947

Sun, W., Fish, J., 2021. Coupling of non-ordinary state-based peridynamics an

d finite element method for fracture propagation in saturated porous media. Int. J. Numer. Anal. Met. 45 (9), 1260-1281. https://doi.org/10.1002/nag.3200

Suzuki, K., Namba, K., Watanabe, Y., 2016. Visualization of high-speed impact of penetrator into icy target. J. Flow Control, Measurement & Visualization 4 (2), 56-69. https://doi.org/10.4236/jfcmv.2016.42006

Toussaint, G., Polyzois, I., 2019. Steel spheres impact on alumina ceramic tiles: Experiments and finite element simulations. Int. J. Appl. Ceram. Tec. 16 (6), 2131-2152. https://doi.org/10.1111/ijac.13318

Wang, C., Xiong, W., Chang, X., Ye, L., Li, X., 2018a. Analysis of variable working conditions for propeller-ice interaction. Ocean Eng. 156, 277-293. https://doi.org/10.1016/j.oceaneng.2018.02.026

Wang, J., Derradji-Aouat, A., 2010. Ship Performance in Broken Ice Floes – Preliminary Numerical Simulations. TR-2010-24. Institute for Ocean Technology, National Research Council, St. John's, NL, Canada. https://doi.org/10.4224/17210723

Wang, Q., Wang, Y., Yuan, L.H., Lu, W., Zhang, Y.H., 2018b. Simulation of brittle-ice contacting with stiffened plate with peridynamics. J. Ship Mech. 22 (3). https://doi.org/10.3969/j.issn.1007-7294.2018.03.008

Wang, Q., Wang, Y., Zan, Y.F., Lu, W., Bai, X., Guo, J., 2018c. Peridynamics simulation of the fragmentation of ice cover by blast loads of an underwater explosion. J. Mar. Sci. Tech. 23, 52-66. https://doi.org/10.1007/s00773-01

7-0454-x

Wu, L.W, Huang, D., Xu, Y., Wang, L., 2020. A rate-dependent dynamic dama ge model in peridynamics for concrete under impact loading. Int. J. Dama ge Mech. 29 (7), 1035-1058. https://doi.org/10.1177/1056789519901162

Yang, D., He, X., Liu, X., Deng, Y., Huang, X., 2020. A peridynamics-based c ohesive zone model (PD-CZM) for predicting cohesive crack propagation. Int. J. Mech. Sci. 184, 105830. https://doi.org/10.1016/j.ijmecsci.2020.10583 0

Zhang, N., Ma, Q., Zheng, X., Yan, S., 2023a. A two-way coupling method fo r simulating wave-induced breakup of ice floes based on SPH. J. Comput. Phys. 488, 112185. https://doi.org/10.1016/j.jcp.2023.112185

Zhang, N., Zheng, X., Ma, Q., Hu, Z., 2019. A numerical study on ice failure process and ice-ship interactions by Smoothed Particle Hydrodynamics. Int. J. Nav. Arch. Ocean 11 (2), 796-808. https://doi.org/10.1016/j.ijnaoe.2019.0 2.008

Zhang, Y.H., Liu, R.W., Yuan, L.H., Li, J.B., Jing, C.Y., Han, D.F., 2023b. Ice breaking by low-velocity impact with a rigid sphere. Int. J. Impact Eng. (under review)

Zhang, Y.H., Wang, Q., Han, D.F., Li, J.B., Wang, C.Y., 2023c. Investigation o n the mixed mode fracture toughness of freshwater ice using the semi-circ ular bend method. Cold Regions Sci. Techno. 205, 103718. https://doi.org/1 0.1016/j.coldregions.2022.103718

Zhang, Y.H., Wang, Q., Han, D.F., Xue, Y.Z., Lu, S.C., Wang, P.G., 2020. Dynamic splitting tensile behaviours of distilled-water and river-water ice using a modified SHPB setup. Int. J. Impact Eng. 145, 103686. https://doi.org/10.1016/j.ijimpeng.2020.103686

Zhang, Y.H., Wang, Q., Han, D.F., Xue, Y.Z., Qu, J., Yao, H.Q., 2021. Experimental study of the quasi-static and dynamic fracture toughness of freshwater ice using notched semi-circular bend method. Eng. Fract. Mech. 247, 107696. https://doi.org/10.1016/j.engfracmech.2021.107696

Zhu, F., Zhao, J., 2021. Peridynamic modelling of blasting induced rock fractures. J. Mech. Phys. Solids 153, 104469. https://doi.org/10.1016/j.jmps.2021.104469